INTERNATIONAL JOURNAL FOR NUMERICAL METHODS IN ENGINEERING
Int. J. Numer. Meth. Engng 2011; **88**:1152–1174
Published online 28 April 2011 in Wiley Online Library (wileyonlinelibrary.com). DOI: 10.1002/nme.3213

p-FEMs for hyperelastic anisotropic nearly incompressible materials under finite deformations with applications to arteries simulation

Zohar Yosibash*, † and Elad Priel

Pearlstone Center for Aeronautical Studies, Department of Mechanical Engineering, Ben-Gurion University of the Negev, Beer-Sheva, Israel

SUMMARY

The displacement-formulation of *p*-FEMs is extended to nearly incompressible hyper-elastic anisotropic materials under finite deformations in a three-dimensional setting. To demonstrate the efficiency and accuracy of the formulation, we derive analytical solutions that serve for the verification of the *p*-FE results. The locking-free properties at the limit of incompressibility, the high convergence rates and the robustness with respect to large aspect ratios of the *p*-FEs are demonstrated by numerical experiments and compared (in terms of degrees of freedom and CPU times) to equivalent classical formulations using *h*-FEMs.

p-FEMs are then exploited to investigate artery-like structures having complex constitutive models and particularly the influence of slight allowable compressibility (of orders of several percents) on the stress levels. Copyright © 2011 John Wiley & Sons, Ltd.

Received 28 December 2010; Accepted 18 March 2011

KEY WORDS: *p*-FEM; artery; locking-free; nearly incompressible Neo-Hookean material; finite strains; hyper-elasticity

1. INTRODUCTION

The *p*-version of the finite element method (*p*-FEM) based on the displacement-formulation has been shown to be efficient in the framework of finite deformations for isotropic hyperelastic materials [1, 2]. Furthermore, in a recent study we demonstrated that the locking-free property of displacement-formulation of *p*-FEMs noted in linear nearly incompressible problems carries over to finite-deformation analyses of nearly incompressible Neo-Hookean and isotropic hyperelastic materials [3]. These advantages in addition to the robustness of the *p*-FEM with respect to large aspect ratios and distortion of the elements makes it especially attractive for modeling biological tissues as arteries.

Arteries are inherently anisotropic and almost incompressible and constructed of several thin layers each having different material properties. A well-accepted *incompressible* hyper-elastic constitutive model for the description of arteries is the fiber-reinforced model introduced by Holzapfel *et al.* [4, 5]. The incompressibility assumption is supported by experimental observations in [6], however, more recent experimental observations show a slight compressibility (for example, in [7] a 3% change in volume is reported). Thus, we complement the aforementioned strain energy

*Correspondence to: Zohar Yosibash, Department of Mechanical Engineering, Ben-Gurion University of the Negev, Beer-Sheva 84105, Israel.
†E-mail: zohary@bgu.ac.il

density function (SEDF) by a 'compressible' part divided by a bulk modulus because it describes a compressible deformation becoming increasingly more incompressible as the bulk modulus tends to ∞. Two similar, yet a bit different SEDFs are introduced by Holzapfel and co-workers to model the fibers, which account for the anisotropic effects, and herein we investigate their difference by several numerical examples at the limit of incompressibility.

To assess the efficiency and accuracy of p-FEMs for such anisotropic hyperelastic constitutive models, we first construct a set of benchmark problems with analytical solutions against which the p-FE results are evaluated. We then compare the performance of the p-FEM with that of the commercial h-FE code Abaqus [8] both in terms of degrees of freedom (DOFs) as well as CPU times, and investigate the mechanical response of an artery-like structure with or without the assumption of incompressibility.

In Section 2, the notation, constitutive model and weak formulation are provided followed by the discretization in the context of p-FEMs. Several simplified example problems for which an exact solution was derived are summarized in Section 3 and used as benchmark problems to verify the accuracy and efficiency of the p-FE implementation compared to the commercial h-FE code Abaqus [8]. An example problem representing a typical mono-layered and bi-layered arteries is considered in Section 4, where we also investigate the nearly incompressible influence on the results. We conclude with a summary and conclusions in Section 5.

2. NOTATIONS AND THE CONSTITUTIVE MODEL

The point of departure is a brief description of our notations for a fiber-reinforced hyper-elastic material. The basic quantity is the deformation gradient $\boldsymbol{F}=\mathrm{Grad}\boldsymbol{\varphi}(\boldsymbol{X},t)=\partial\varphi^k(X^1,X^2,X^3,t)/\partial X^K\boldsymbol{g}_i\otimes\boldsymbol{G}^K$, where $\boldsymbol{x}=\boldsymbol{\varphi}(\boldsymbol{X},t)$ defines the placement of the point $\boldsymbol{X}$ at time t. X^K, $k=1,2,3$, are the material (reference) (curvilinear) coordinates, $\boldsymbol{g}_i$ are the tangent and $\boldsymbol{G}^K$ the gradient vectors in the current and the reference configuration. Usually, the displacement vector $\boldsymbol{U}(\boldsymbol{X},t)\overset{\mathrm{def}}{=}(U_X,U_Y,U_Z)^{\mathrm{T}}$ is introduced, i.e. $\boldsymbol{x}=\boldsymbol{X}+\boldsymbol{U}(\boldsymbol{X},t)$, and with this notation $\boldsymbol{F}=\boldsymbol{I}+\mathrm{Grad}\boldsymbol{U}(\boldsymbol{X},t)$. We interchange X^1, X^2, X^3 with X, Y, Z when appropriate for the Cartesian coordinate system.

For a general strain-energy function for an isotropic hyper-elastic material with two families of fibers, following Holzapfel and Gasser [4], $\psi(\boldsymbol{C},\hat{\boldsymbol{M}}_0,\hat{\boldsymbol{M}}_1)=\Psi(\mathrm{I}_{\boldsymbol{C}},\mathrm{II}_{\boldsymbol{C}},\mathrm{III}_{\boldsymbol{C}},\mathrm{IV}_{\boldsymbol{C}},\mathrm{VI}_{\boldsymbol{C}})$ depends on the invariants of the right Cauchy–Green tensor $\boldsymbol{C}=\boldsymbol{F}^{\mathrm{T}}\boldsymbol{F}=(\boldsymbol{I}+\mathrm{Grad}\boldsymbol{U})^{\mathrm{T}}(\boldsymbol{I}+\mathrm{Grad}\boldsymbol{U})$, and two direction vectors along fiber directions $\hat{\boldsymbol{M}}_0$, and $\hat{\boldsymbol{M}}_1$. For example, using the Cartesian coordinate system in Figure 1, the fiber directions are $\hat{\boldsymbol{M}}_0=(\sin\beta,-\cos\beta Y/(\sqrt{Y^2+Z^2}),\cos\beta Z/(\sqrt{Y^2+Z^2}))^{\mathrm{T}}$, $\hat{\boldsymbol{M}}_1=(-\sin\beta,-\cos\beta Y/(\sqrt{Y^2+Z^2}),\cos\beta Z/(\sqrt{Y^2+Z^2}))^{\mathrm{T}}$.

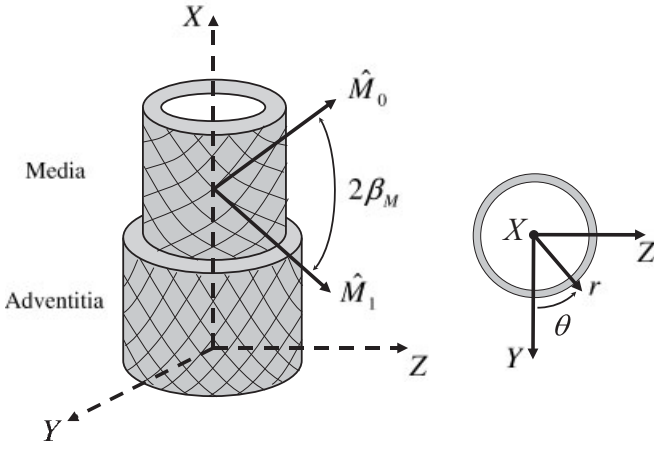

Figure 1. Coordinate system in a typical artery.

DOI: 10.1002/nme

The invariants of the Cauchy–Green tensor are

$$\mathrm{I}_{\boldsymbol{C}}=\mathrm{tr}\boldsymbol{C},\quad \mathrm{II}_{\boldsymbol{C}}=\tfrac{1}{2}((\mathrm{tr}\boldsymbol{C})^2-\mathrm{tr}\boldsymbol{C}^2),\quad \mathrm{III}_{\boldsymbol{C}}=\det\boldsymbol{C}=(\det\boldsymbol{F})^2\overset{\mathrm{def}}{=}J^2, \tag{1}$$

where $\mathrm{tr}\boldsymbol{C}=C_N^N$ symbolizes the trace operator and the invariants that represent stretch in the fiber directions are

$$\mathrm{IV}_{\boldsymbol{C}}=\hat{\boldsymbol{M}}_0\cdot\boldsymbol{C}\cdot\hat{\boldsymbol{M}}_0,\quad \mathrm{VI}_{\boldsymbol{C}}=\hat{\boldsymbol{M}}_1\cdot\boldsymbol{C}\cdot\hat{\boldsymbol{M}}_1. \tag{2}$$

The second Piola-Kirchhoff stress tensor is formulated with quantities relative to the reference configuration

$$\boldsymbol{S}=2\frac{\mathrm{d}\psi(\boldsymbol{C})}{\mathrm{d}\boldsymbol{C}}=\delta_0\boldsymbol{I}+\delta_1\boldsymbol{C}+\delta_2\boldsymbol{C}^{-1}+\delta_4\hat{\boldsymbol{M}}_0\otimes\hat{\boldsymbol{M}}_0+\delta_6\hat{\boldsymbol{M}}_1\otimes\hat{\boldsymbol{M}}_1, \tag{3}$$

which result from the application of the chain rule, with

$$\delta_0=2\left(\frac{\partial\Psi}{\partial\mathrm{I}_{\boldsymbol{C}}}+\mathrm{I}_{\boldsymbol{C}}\frac{\partial\Psi}{\partial\mathrm{II}_{\boldsymbol{C}}}\right),\quad \delta_1=-2\frac{\partial\Psi}{\partial\mathrm{II}_{\boldsymbol{C}}},\quad \delta_2=2\mathrm{III}_{\boldsymbol{C}}\frac{\partial\Psi}{\partial\mathrm{III}_{\boldsymbol{C}}},\quad \delta_4=2\frac{\partial\Psi}{\partial\mathrm{IV}_{\boldsymbol{C}}},\quad \delta_6=2\frac{\partial\Psi}{\partial\mathrm{VI}_{\boldsymbol{C}}}. \tag{4}$$

In (3) use is made of

$$\frac{\mathrm{dI}_{\boldsymbol{C}}}{\mathrm{d}\boldsymbol{C}}=\boldsymbol{I},\quad \frac{\mathrm{dII}_{\boldsymbol{C}}}{\mathrm{d}\boldsymbol{C}}=\mathrm{I}_{\boldsymbol{C}}\boldsymbol{I}-\boldsymbol{C},\quad \frac{\mathrm{dIII}_{\boldsymbol{C}}}{\mathrm{d}\boldsymbol{C}}=\mathrm{III}_{\boldsymbol{C}}\boldsymbol{C}^{-1}=adj\boldsymbol{C},\quad \frac{\mathrm{dIV}_{\boldsymbol{C}}}{\mathrm{d}\boldsymbol{C}}=\hat{\boldsymbol{M}}_0\otimes\hat{\boldsymbol{M}}_0,\quad \frac{\mathrm{dVI}_{\boldsymbol{C}}}{\mathrm{d}\boldsymbol{C}}=\hat{\boldsymbol{M}}_1\otimes\hat{\boldsymbol{M}}_1. \tag{5}$$

We consider a strain-energy density function composed of three parts, an isochoric isotropic and a volumetric isotropic Neo-Hookean parts, and a transversely isotropic part representing the collagen fibers:

$$\psi(\boldsymbol{C})=[\psi_{\mathrm{isoch}}(\boldsymbol{C})+\psi_{\mathrm{vol}}(\boldsymbol{C})]+\psi_{\mathrm{fibers}}(\boldsymbol{C}). \tag{6}$$

The isotropic part of the SEDF is a nearly incompressible Neo-Hookean SEDF:

$$\Psi_{\mathrm{iso}}=c_1(\mathrm{I}_{\overline{\boldsymbol{C}}}-3)+\frac{1}{D_1}(J-1)^2=c_1(\mathrm{I}_{\boldsymbol{C}}\mathrm{III}_{\boldsymbol{C}}^{-1/3}-3)+\frac{1}{D_1}(\mathrm{III}_{\boldsymbol{C}}^{1/2}-1)^2. \tag{7}$$

c_1 and D_1 are constants related to the shear modulus μ and to the bulk modulus κ.

$$c_1=\frac{\mu}{2},\quad D_1=\frac{2}{\kappa} \tag{8}$$

For the transversely isotropic part of the SEDF, representing the collagen fibers, two variations are considered [4, 5], either

$$\begin{aligned}\Psi_{1,\mathrm{fibers}}=&\frac{k_1}{2k_2}[\exp[k_2(\mathrm{IV}_{\boldsymbol{C}}J^{-\frac{2}{3}}-1)^2]-1]\\&+\frac{k_1}{2k_2}[\exp[k_2(\mathrm{VI}_{\boldsymbol{C}}J^{-\frac{2}{3}}-1)^2]-1],\quad \mathrm{IV}_{\boldsymbol{C}},\mathrm{VI}_{\boldsymbol{C}}\geqslant 1\end{aligned} \tag{9}$$

or

$$\begin{aligned}\Psi_{2,\mathrm{fibers}}(\boldsymbol{C})=&\frac{k_1}{2k_2}[\exp[k_2(\mathrm{IV}_{\boldsymbol{C}}-1)^2]-1]\\&+\frac{k_1}{2k_2}[\exp[k_2(\mathrm{VI}_{\boldsymbol{C}}-1)^2]-1],\quad \mathrm{IV}_{\boldsymbol{C}},\mathrm{VI}_{\boldsymbol{C}}\geqslant 1.\end{aligned} \tag{10}$$

Both SEDFs (9) and (10) appear in different publications by the same authors without a clear explanation on which to use. The SEDF $\Psi_{1,\mathrm{fibers}}$ is expressed in terms of the unimodular Cauchy–Green tensor $\overline{\boldsymbol{C}}$ (see below), implying the incompressibility of the fibers. Because the fibers cannot

DOI: 10.1002/nme

support compressive loads, the anisotropic part is omitted for any point at which $\mathrm{IV}_{\boldsymbol{C}}$, $\mathrm{VI}_{\boldsymbol{C}}<1$. $\mathrm{I}_{\overline{\boldsymbol{C}}}=\mathrm{I}_{\boldsymbol{C}}\mathrm{III}_{\boldsymbol{C}}^{-1/3}=\mathrm{I}_{\boldsymbol{C}}J^{-2/3}$ defines the first invariant of the unimodular right Cauchy–Green tensor $\overline{\boldsymbol{C}}=(\det\boldsymbol{C})^{-1/3}\boldsymbol{C}$ resulting from the multiplicative decomposition of the deformation gradient into a volumetric and an isochoric part (see [9] and the literature cited therein).

The second Piola-Kirchhoff (P-K) stress tensor is obtained by

$$\boldsymbol{S}=2\frac{\partial\Psi}{\partial\boldsymbol{C}}=2\frac{\partial\Psi_{\mathrm{isoch}}}{\partial\boldsymbol{C}}+2\frac{\partial\Psi_{\mathrm{vol}}}{\partial\boldsymbol{C}}+2\frac{\partial\Psi_{\mathrm{fibers}}}{\partial\boldsymbol{C}}\overset{\mathrm{def}}{=}\underbrace{\boldsymbol{S}_{\mathrm{isoch}}+\boldsymbol{S}_{\mathrm{vol}}}_{\boldsymbol{S}_{\mathrm{iso}}}+\boldsymbol{S}_{\mathrm{fibers}},\tag{11}$$

where

$$\boldsymbol{S}_{\mathrm{isoch}}=-\tfrac{2}{3}J^{-2/3}c_1\boldsymbol{C}^{-1}\mathrm{I}_{\boldsymbol{C}}+2J^{-2/3}c_1\boldsymbol{I},\tag{12}$$

$$\boldsymbol{S}_{\mathrm{vol}}=\frac{2J^2}{D_1}\boldsymbol{C}^{-1}-\frac{2J}{D_1}\boldsymbol{C}^{-1},\tag{13}$$

$$\begin{aligned}\boldsymbol{S}_{1,\mathrm{fibers}}=2k_1J^{-\frac{2}{3}}[&(1-\mathrm{IV}_{\boldsymbol{C}}J^{-\frac{2}{3}})(\tfrac{1}{3}\mathrm{IV}_{\boldsymbol{C}}\boldsymbol{C}^{-1}-\hat{\boldsymbol{M}}_0\otimes\hat{\boldsymbol{M}}_0)e^{k_2(\mathrm{IV}_{\boldsymbol{C}}J^{-\frac{2}{3}}-1)^2}\\&+(1-\mathrm{VI}_{\boldsymbol{C}}J^{-\frac{2}{3}})(\tfrac{1}{3}\mathrm{VI}_{\boldsymbol{C}}\boldsymbol{C}^{-1}-\hat{\boldsymbol{M}}_1\otimes\hat{\boldsymbol{M}}_1)e^{k_2(\mathrm{VI}_{\boldsymbol{C}}J^{-\frac{2}{3}}-1)^2}],\end{aligned}\tag{14}$$

$$\boldsymbol{S}_{2,\mathrm{fibers}}=2k_1[(\mathrm{IV}_{\boldsymbol{C}}-1)\hat{\boldsymbol{M}}_0\otimes\hat{\boldsymbol{M}}_0e^{k_2(\mathrm{IV}_{\boldsymbol{C}}-1)^2}+(\mathrm{VI}_{\boldsymbol{C}}-1)\hat{\boldsymbol{M}}_1\otimes\hat{\boldsymbol{M}}_1e^{k_2(\mathrm{VI}_{\boldsymbol{C}}-1)^2}].\tag{15}$$

Remark 2.1

At the limit of incompressibility ($J\to1$), then $\Psi_{1,\mathrm{fibers}}\xrightarrow{J\to1}\Psi_{2,\mathrm{fibers}}$. However, inspecting (14) and (15) $(\boldsymbol{S}_{1,\mathrm{fibers}}-\boldsymbol{S}_{2,\mathrm{fibers}})\overset{J\to1}{\nrightarrow}0$ and a difference exists also at the incompressibility limit:

$$\boldsymbol{S}_{1,\mathrm{fibers}}-\boldsymbol{S}_{2,\mathrm{fibers}}\overset{J\to1}{=}\tfrac{2}{3}k_1[\mathrm{IV}_{\boldsymbol{C}}(1-\mathrm{IV}_{\boldsymbol{C}})e^{k_2(\mathrm{IV}_{\boldsymbol{C}}-1)^2}+\mathrm{VI}_{\boldsymbol{C}}(1-\mathrm{VI}_{\boldsymbol{C}})e^{k_2(\mathrm{VI}_{\boldsymbol{C}}-1)^2}]\boldsymbol{C}^{-1}.\tag{16}$$

As noticed in (16), at the limit of incompressibility, the difference in the second P-K stress tensors becomes progressively more prominent as the stretch in the fiber direction increases because of $\mathrm{VI}_{\boldsymbol{C}}$ and $\mathrm{IV}_{\boldsymbol{C}}$; however, at the same time it decreases due to the term $\boldsymbol{C}^{-1}$. Numerical experiments provided in the sequel discuss the difference in the models as $J\to1$.

The fourth-order tangent tensor $\mathbb{C}\overset{\mathrm{def}}{=}2\partial\boldsymbol{S}/\partial\boldsymbol{C}=\mathbb{C}_{\mathrm{iso}}+\mathbb{C}_{\mathrm{fibers}}$ required in the framework of the consistent linearization is a sum of the isotropic part and the fibers. The contribution of the isotropic part is

$$\begin{aligned}\mathbb{C}_{iso}=&-\frac{4}{3}c_1J^{-\frac{2}{3}}\left[\boldsymbol{C}^{-1}\otimes\boldsymbol{I}+\boldsymbol{I}\otimes\boldsymbol{C}^{-1}-\frac{1}{3}\mathrm{I}_{\boldsymbol{C}}\boldsymbol{C}^{-1}\otimes\boldsymbol{C}^{-1}+\mathrm{I}_{\boldsymbol{C}}\frac{\partial\boldsymbol{C}^{-1}}{\partial\boldsymbol{C}}\right]\\&+\frac{2}{D_1}J\left[(2J-1)\boldsymbol{C}^{-1}\otimes\boldsymbol{C}^{-1}+2(J-1)\frac{\partial\boldsymbol{C}^{-1}}{\partial\boldsymbol{C}}\right],\end{aligned}\tag{17}$$

whereas the fibers' part is

$$\mathbb{C}_{1,\mathrm{fibers}}=\tfrac{4}{3}k_1J^{-\frac{2}{3}}e^{k_2(\mathrm{IV}_{\boldsymbol{C}}J^{-\frac{2}{3}}-1)^2}\{-[J^{-\frac{2}{3}}+2\mathrm{IV}_{\boldsymbol{C}}k_2(\mathrm{IV}_{\boldsymbol{C}}J^{-\frac{2}{3}}-1)+1]\tag{18}$$

$$\times[(\hat{\boldsymbol{M}}_0\otimes\hat{\boldsymbol{M}}_0)\otimes\boldsymbol{C}^{-1}+\boldsymbol{C}^{-1}\otimes(\hat{\boldsymbol{M}}_0\otimes\hat{\boldsymbol{M}}_0)]\tag{19}$$

$$+\frac{2}{3}\mathrm{IV}_{\boldsymbol{C}}[2\mathrm{IV}_{\boldsymbol{C}}J^{-\frac{2}{3}}(1+k_2(\mathrm{IV}_{\boldsymbol{C}}J^{-\frac{2}{3}}-1)^2)-1](\boldsymbol{C}^{-1})\otimes(\boldsymbol{C}^{-1})$$

DOI: 10.1002/nme

$$
\begin{aligned}
&+\mathrm{IV}_{\boldsymbol{C}}(1-\mathrm{IV}_{\boldsymbol{C}}J^{-\frac{2}{3}})\left(\frac{\partial \boldsymbol{C}^{-1}}{\partial \boldsymbol{C}}\right)\\
&+3J^{-\frac{2}{3}}(1+2k_2(\mathrm{IV}_{\boldsymbol{C}}J^{-\frac{2}{3}})^2)(\hat{\boldsymbol{M}}_0\otimes\hat{\boldsymbol{M}}_0)\otimes(\hat{\boldsymbol{M}}_0\otimes\hat{\boldsymbol{M}}_0)\}\\
&+\tfrac{4}{3}k_1J^{-\frac{2}{3}}e^{k_2(\mathrm{VI}_{\boldsymbol{C}}J^{-\frac{2}{3}}-1)^2}\{-[J^{-\frac{2}{3}}+2\mathrm{VI}_{\boldsymbol{C}}k_2(\mathrm{VI}_{\boldsymbol{C}}J^{-\frac{2}{3}}-1)+1] \qquad (20)\\
&\times[(\hat{\boldsymbol{M}}_1\otimes\hat{\boldsymbol{M}}_1)\otimes\boldsymbol{C}^{-1}+\boldsymbol{C}^{-1}\otimes(\hat{\boldsymbol{M}}_1\otimes\hat{\boldsymbol{M}}_1)] \qquad (21)\\
&+\frac{2}{3}\mathrm{VI}_{\boldsymbol{C}}[2\mathrm{VI}_{\boldsymbol{C}}J^{-\frac{2}{3}}(1+k_2(\mathrm{VI}_{\boldsymbol{C}}J^{-\frac{2}{3}}-1)^2)-1](\boldsymbol{C}^{-1})\otimes(\boldsymbol{C}^{-1})\\
&+\mathrm{VI}_{\boldsymbol{C}}(1-\mathrm{VI}_{\boldsymbol{C}}J^{-\frac{2}{3}})\left(\frac{\partial \boldsymbol{C}^{-1}}{\partial \boldsymbol{C}}\right)\\
&+3J^{-\frac{2}{3}}(1+2k_2(\mathrm{VI}_{\boldsymbol{C}}J^{-\frac{2}{3}})^2)(\hat{\boldsymbol{M}}_1\otimes\hat{\boldsymbol{M}}_1)\otimes(\hat{\boldsymbol{M}}_1\otimes\hat{\boldsymbol{M}}_1)\}
\end{aligned}
$$

or

$$
\begin{aligned}
\mathbb{C}_{2,\mathrm{fibers}} &= 4k_1e^{k_2(\mathrm{IV}_{\boldsymbol{C}}-1)^2}[(1+2k_2(\mathrm{IV}_{\boldsymbol{C}}-1)^2)(\hat{\boldsymbol{M}}_0\otimes\hat{\boldsymbol{M}}_0)\otimes(\hat{\boldsymbol{M}}_0\otimes\hat{\boldsymbol{M}}_0)]\\
&\quad+4k_1e^{k_2(\mathrm{VI}_{\boldsymbol{C}}-1)^2}[(1+2k_2(\mathrm{VI}_{\boldsymbol{C}}-1)^2)(\hat{\boldsymbol{M}}_1\otimes\hat{\boldsymbol{M}}_1)\otimes(\hat{\boldsymbol{M}}_1\otimes\hat{\boldsymbol{M}}_1)] \qquad (22)
\end{aligned}
$$

with $(\partial\boldsymbol{C}^{-1}/\partial\boldsymbol{C})_{IJKL}=-(\boldsymbol{C}^{-1})_{IK}(\boldsymbol{C}^{-1})_{JL}$.

2.1. Weak formulation and discretization by p-FEs

The weak formulation expressed in the reference configuration, neglecting inertia terms (also denoted by the total-Lagrange formulation) is obtained by a standard linearization of the non-linear weak form, see e.g. [10], followed by a Newton–Raphson iterative scheme. Assuming that the displacements are known at a given instance, $\boldsymbol{U}^{(k)}$, then after applying a load increment, one is interested in the associated displacement increment denoted by $\Delta\boldsymbol{U}$. Once $\Delta\boldsymbol{U}$ is computed a new displacement vector is generated

$$\boldsymbol{U}^{(k+1)}=\boldsymbol{U}^{(k)}+\Delta\boldsymbol{U} \qquad (23)$$

and the iterative scheme is continued.

Remark 2.2

For convergence, Newton's iterative scheme requires an initial guess in the vicinity of the solution. Thus, a further iteration loop is introduced by dividing the load into several load steps, so that the iterations on k start at each load step with an initial solution being the solution at the previous load step.

Having $\boldsymbol{U}^{(k)}$, the associated deformation gradient may be computed $\boldsymbol{F}^{(k)}\overset{\mathrm{def}}{=}\boldsymbol{I}+(\partial\boldsymbol{U}^{(k)}/\partial\boldsymbol{X})$. The linearized system to be solved is [10, p. 148]

$$\text{Find } \Delta\boldsymbol{U}\in\mathscr{E}(\Omega_0)\quad \text{such that } \forall\boldsymbol{Q}\in\mathscr{E}(\Omega_0)$$

$$
\begin{aligned}
&\frac{1}{4}\int_{\Omega_0}\left[\frac{\partial\boldsymbol{Q}}{\partial\boldsymbol{X}}\cdot\boldsymbol{F}^{(k)}+\boldsymbol{F}^{(k)}\cdot\frac{\partial\boldsymbol{Q}}{\partial\boldsymbol{X}}\right]:\mathbb{C}^{(k)}:\left[\frac{\partial\Delta\boldsymbol{U}}{\partial\boldsymbol{X}}\cdot\boldsymbol{F}^{(k)}+\boldsymbol{F}^{(k)}\cdot\frac{\partial\Delta\boldsymbol{U}}{\partial\boldsymbol{X}}\right]\mathrm{d}\Omega_0\\
&\quad+\int_{\Omega_0}\boldsymbol{S}(\boldsymbol{U}^{(k)}):\left(\frac{\partial\Delta\boldsymbol{U}}{\partial\boldsymbol{X}}\cdot\frac{\partial\boldsymbol{Q}}{\partial\boldsymbol{X}}\right)\mathrm{d}\Omega_0+DG(\Delta\boldsymbol{U},\boldsymbol{Q})\\
&=\int_{\partial\Omega_0}\boldsymbol{t}^{(N)}\cdot\boldsymbol{Q}\,d\Gamma_0+G(\boldsymbol{Q})-\frac{1}{2}\int_{\Omega_0}\boldsymbol{S}(\boldsymbol{U}^{(k)}):\left[\left(\frac{\partial\boldsymbol{Q}}{\partial\boldsymbol{X}}\right)\cdot\boldsymbol{F}^{(k)}+(\boldsymbol{F}^{(k)})\cdot\frac{\partial\boldsymbol{Q}}{\partial\boldsymbol{X}}\right]\mathrm{d}\Omega_0 \qquad (24)
\end{aligned}
$$

DOI: 10.1002/nme

with $\boldsymbol{t}^{(N)}=\boldsymbol{FS}\cdot\hat{\boldsymbol{N}}$ being the traction applied on the reference configuration boundary. The terms $DG(\Delta\boldsymbol{U},\boldsymbol{Q})$ and $G(\boldsymbol{Q})$ are to be added if pressure (follower loads) are considered, see Equations (49) and (53) in [2].

Remark 2.3
In our p-FEM implementation, $\mathbb{C}$ is computed at each iteration step, unlike the modified Newton methods in which $\mathbb{C}$ is computed only once for each load increment or once for every several equilibrium iterations.

2.2. *p-FEM implementation for 3D domains*

The weak form (24) is discretized using a space of hierarchical polynomials (shape functions) $N_i(\xi,\eta,\zeta)$ on the standard hexahedral element (see [11]). The sought (trial) vector $\Delta\boldsymbol{U}$ is represented by an unknown $3n\times 1$ vector $\Delta\hat{\boldsymbol{U}}$ as follows:

$$\Delta\boldsymbol{U}=\begin{bmatrix} N_1\cdots N_n & 0\cdots 0 & 0\cdots 0 \\ 0\cdots 0 & N_1\cdots N_n & 0\cdots 0 \\ 0\cdots 0 & 0\cdots 0 & N_1\cdots N_n \end{bmatrix}\Delta\hat{\boldsymbol{U}}\overset{\text{def}}{=}[N]\Delta\hat{\boldsymbol{U}} \tag{25}$$

whereas $\boldsymbol{Q}\overset{\text{def}}{=}[N]\hat{\boldsymbol{Q}}$ is the test vector. Using blending-mapping functions $\Gamma(\xi,\eta,\zeta)$ from the standard element to the physical element [12], an *exact geometry description of the faces and edges* of the physical element is obtained

$$\boldsymbol{X}=\begin{Bmatrix} X \\ Y \\ Z \end{Bmatrix}=\begin{Bmatrix} \Gamma_1(\xi,\eta,\zeta) \\ \Gamma_2(\xi,\eta,\zeta) \\ \Gamma_3(\xi,\eta,\zeta) \end{Bmatrix},\quad [\mathscr{J}]=\begin{bmatrix} \dfrac{\partial\Gamma_1}{\partial\xi} & \dfrac{\partial\Gamma_2}{\partial\xi} & \dfrac{\partial\Gamma_3}{\partial\xi} \\ \dfrac{\partial\Gamma_1}{\partial\eta} & \dfrac{\partial\Gamma_2}{\partial\eta} & \dfrac{\partial\Gamma_3}{\partial\eta} \\ \dfrac{\partial\Gamma_1}{\partial\zeta} & \dfrac{\partial\Gamma_2}{\partial\zeta} & \dfrac{\partial\Gamma_3}{\partial\zeta} \end{bmatrix}. \tag{26}$$

Derivatives of the shape functions in the standard element are computed as:

$$\frac{\partial N_i}{\partial\boldsymbol{X}}=\begin{Bmatrix} \dfrac{\partial N_i}{\partial X} \\ \dfrac{\partial N_i}{\partial Y} \\ \dfrac{\partial N_i}{\partial Z} \end{Bmatrix}=[\mathscr{J}]^{-1}\begin{Bmatrix} \dfrac{\partial N_i}{\partial\xi} \\ \dfrac{\partial N_i}{\partial\eta} \\ \dfrac{\partial N_i}{\partial\zeta} \end{Bmatrix}. \tag{27}$$

Remark 2.4
It is important to realize that the use of the total-Lagrange formulation does not require to update the FE mesh, and hence the Jacobian $[\mathscr{J}]$ is determined once, relative to the material (undeformed) configuration. The updates from one iteration to the next are performed by updating the integrand terms due to the update of the displacements (23).

By using (27) with (25) and (26) the discretized form of (24) is obtained. The right-hand side of (24) results in the 'out-of-balance' vector, whereas the left-hand side is denoted by the 'tangent-stiffness-matrix'.

2.3. *The out-of-balance vector*

Neglecting inertial forces the out-of-balance vector consists of three parts $\boldsymbol{r}^{ob}=\boldsymbol{r}^{\text{Ext}}+\boldsymbol{r}^{\text{Follwer}}-\boldsymbol{r}^{\text{Int}}$ with $\boldsymbol{r}^{\text{Follwer}}$ (given in [2, Equation (49)]) is considered only when follower loads are present.

DOI: 10.1002/nme

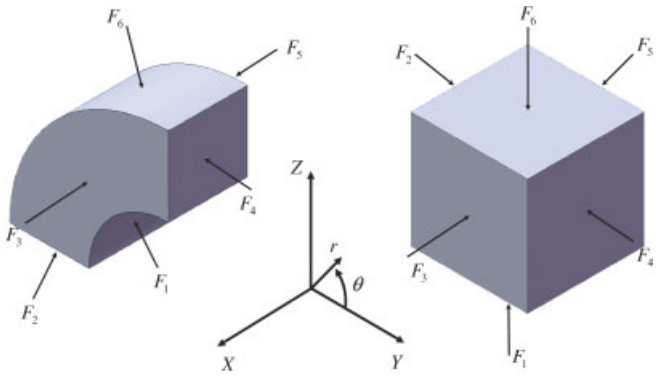

Figure 2. Face labeling.

Considering for example an element with traction $\vec{t}$ applied on face number 6 and a pressure P applied on face number 1 (see Figure 2), the following contributions to the out-of-balance vector are evident:

$$(r^{\mathrm{Ext}})_\ell = \int_{-1}^{1}\int_{-1}^{1} t_k N_{k\ell}\sqrt{A\cdot B - C^2}\Big|_{\zeta=1} \mathrm{d}\xi\,\mathrm{d}\eta,$$

$$A = \left(\frac{\partial\Gamma_1}{\partial\xi}\right)^2 + \left(\frac{\partial\Gamma_2}{\partial\xi}\right)^2 + \left(\frac{\partial\Gamma_3}{\partial\xi}\right)^2,$$

$$B = \left(\frac{\partial\Gamma_1}{\partial\eta}\right)^2 + \left(\frac{\partial\Gamma_2}{\partial\eta}\right)^2 + \left(\frac{\partial\Gamma_3}{\partial\eta}\right)^2,$$

$$C = \frac{\partial\Gamma_1}{\partial\xi}\frac{\partial\Gamma_1}{\partial\eta} + \frac{\partial\Gamma_2}{\partial\xi}\frac{\partial\Gamma_2}{\partial\eta} + \frac{\partial\Gamma_3}{\partial\xi}\frac{\partial\Gamma_3}{\partial\eta}, \tag{28}$$

$$(r^{\mathrm{Int}})_\ell = \int_{-1}^{1}\int_{-1}^{1}\int_{-1}^{1} S_{ij}\frac{1}{2}\left[F_{mj}\frac{\partial N_{m\ell}}{\partial X_i} + F_{mi}\frac{\partial N_{m\ell}}{\partial X_j}\right]\det[\mathscr{J}]\mathrm{d}\xi\,\mathrm{d}\eta\,\mathrm{d}\zeta, \tag{29}$$

$$(r^{\mathrm{Follower}})_\ell = \int_{-1}^{1}\int_{-1}^{1} P[\alpha_m N_{m\ell}]\Big|_{\zeta=-1} \mathrm{d}\xi\,\mathrm{d}\eta, \tag{30}$$

$$\alpha_1 = F_{2j}\frac{\partial\Gamma_j}{\partial\xi}F_{3k}\frac{\partial\Gamma_k}{\partial\eta} - F_{3j}\frac{\partial\Gamma_j}{\partial\xi}F_{2k}\frac{\partial\Gamma_k}{\partial\eta},$$

$$\alpha_2 = F_{3j}\frac{\partial\Gamma_j}{\partial\xi}F_{1k}\frac{\partial\Gamma_k}{\partial\eta} - F_{1j}\frac{\partial\Gamma_j}{\partial\xi}F_{3k}\frac{\partial\Gamma_k}{\partial\eta},$$

$$\alpha_3 = F_{1j}\frac{\partial\Gamma_j}{\partial\xi}F_{2k}\frac{\partial\Gamma_k}{\partial\eta} - F_{2j}\frac{\partial\Gamma_j}{\partial\xi}F_{1k}\frac{\partial\Gamma_k}{\partial\eta},$$

where $N_{m\ell}$ denotes the element in the mth row and ℓth column of the matrix $[N]$, and $\Gamma_i(\xi,\eta,\zeta)$ are the mapping functions from the standard element to the elements in the original configuration (26).

2.4. The tangent stiffness matrix

The 'tangent-stiffness-matrix' consists of three parts $[K^{\mathrm{Tangent}}]=[K_T^{\mathrm{Int,Mat}}+K_T^{\mathrm{Int,Geo}}+K_T^{\mathrm{Follower}}]$ [10] with the third term (see [2, Equation (53)]) only considered cases of follower loads. Considering

DOI: 10.1002/nme

the element discussed in the Section 2.3 one obtains:

$$
\begin{aligned}
(K_T^{\text{Int,Mat}})_{\ell h} &= \int_{-1}^{1}\int_{-1}^{1}\int_{-1}^{1} \frac{1}{4}\left[F_{mj}\frac{\partial N_{m\ell}}{\partial X_i}+F_{mi}\frac{\partial N_{m\ell}}{\partial X_j}\right] \\
&\quad \times \mathbb{C}_{ijab}\left[F_{mb}\frac{\partial N_{mh}}{\partial X_a}+F_{ma}\frac{\partial N_{mh}}{\partial X_b}\right]\det \mathscr{J}\,\mathrm{d}\xi\,\mathrm{d}\eta\,\mathrm{d}\zeta, \\
(K_T^{\text{Int,Geo}})_{\ell h} &= \int_{-1}^{1}\int_{-1}^{1}\int_{-1}^{1} S_{ij}\frac{\partial N_{s\ell}}{\partial X_i}\frac{\partial N_{sh}}{\partial X_j}\det \mathscr{J}\,\mathrm{d}\xi\,\mathrm{d}\eta\,\mathrm{d}\zeta, \\
(K_T^{\text{Follower}})_{\ell h} &= -\int_{-1}^{1}\int_{-1}^{-1} P[\mathscr{B}_{i\ell}N_{ih}]\Big|_{\zeta=-1}\,\mathrm{d}\xi\,\mathrm{d}\eta, \qquad (31) \\
\mathscr{B}_{1\ell} &= F_{2j}\left[\frac{\partial \Gamma_j}{\partial \xi}\frac{\partial N_{3\ell}}{\partial \eta}-\frac{\partial \Gamma_j}{\partial \eta}\frac{\partial N_{3\ell}}{\partial \xi}\right]+F_{3j}\left[\frac{\partial \Gamma_j}{\partial \eta}\frac{\partial N_{2\ell}}{\partial \xi}-\frac{\partial \Gamma_j}{\partial \eta}\frac{\partial N_{2\ell}}{\partial \eta}\right], \\
\mathscr{B}_{2\ell} &= F_{3j}\left[\frac{\partial \Gamma_j}{\partial \xi}\frac{\partial N_{1\ell}}{\partial \eta}-\frac{\partial \Gamma_j}{\partial \eta}\frac{\partial N_{1\ell}}{\partial \xi}\right]+F_{1j}\left[\frac{\partial \Gamma_j}{\partial \eta}\frac{\partial N_{3\ell}}{\partial \xi}-\frac{\partial \Gamma_j}{\partial \eta}\frac{\partial N_{3\ell}}{\partial \eta}\right], \\
\mathscr{B}_{3\ell} &= F_{1j}\left[\frac{\partial \Gamma_j}{\partial \xi}\frac{\partial N_{2\ell}}{\partial \eta}-\frac{\partial \Gamma_j}{\partial \eta}\frac{\partial N_{2\ell}}{\partial \xi}\right]+F_{2j}\left[\frac{\partial \Gamma_j}{\partial \eta}\frac{\partial N_{1\ell}}{\partial \xi}-\frac{\partial \Gamma_j}{\partial \eta}\frac{\partial N_{1\ell}}{\partial \eta}\right].
\end{aligned}
$$

The 'out-of-balance' vector and the 'tangent-stiffness-matrix' are computed at each iteration and the iterative process continues until the relative difference in the 'out-of-balance' vector is smaller than a given tolerance:

$$
\frac{\sqrt{\sum_i (r_i^{\text{Ext}}+r_i^{\text{Follower}}-r_i^{\text{Int}})^2}}{\sqrt{\sum_i (r_i^{\text{Ext}}+r_i^{\text{Follower}})^2}}<\varepsilon, \quad i=1,\ldots,3n.
$$

In all our computations $\varepsilon=10^{-6}$.

For the general case of follower load the linearized system of equations that must be solved at each iteration step is:

$$
[K^{\text{Tangent}}]\Delta\hat{U}=(r^{ob}). \qquad (32)
$$

Remark 2.5

The tangent matrices $K^{\text{Int,Mat}}$ and $K^{\text{Int,Geo}}$ are symmetric [10], whereas K^{Follower} in general is not [10]. Therefore, the bi-conjugate gradient method [13] is utilized for inverting K^{Tangent} and solving (32).

Remark 2.6

The p-FEM code used in this study is not optimized with respect to element numbering. This results in a large bandwidth matrix in the assembly process. A more efficient implementation can be obtained by an optimized element numbering scheme.

3. EXACT SOLUTIONS, VERIFICATION AND ACCURACY OF THE p-FEM

The verification of the p-FE implementation, as well as its accuracy and efficiency for non-linear problems, can only be determined by comparison with exact solutions. Therefore, herein we summarize six exact solutions, denoted as A–D and F–G, i.e. we provide the material properties, domain definition, boundary conditions and the solution itself which serve for verification purposes. Two domains are considered, a cube and a tube, with faces labeled in Figure 2. The number of integration points in each flat-faced hexahedral is $(p+1)^3$, whereas in a cylindrical-shaped hexahedral is $(p+3)^3$. The material properties used represent the human left anterior descending

DOI: 10.1002/nme

(LAD) coronary artery media layer (taken from [14]). For problems (A–D and F–G) $c_1 = 0.027\,\text{MPa}$, $D_1 = 30\,\text{MPa}^{-1}$, with anisotropic parameters $k_1 = 0.00064\,\text{MPa}$, $k_2 = 3.5$ for problems (F–G). In the first four example problems the isotropic SEDF in (7) is considered, representing homogeneous stretch and shear (A–B), a tube under internal and external pressures to verify problems involving a follower load (C), and a stretched cube under distributed body forces and tractions (D) with a complex state of stresses. A fiber-reinforced SEDF given by (7) and (9) is considered in problems F–G. Details on problems A–D are provided in Table I.

Remark 3.1
Tractions are computed using $\boldsymbol{t} = \boldsymbol{FS}\cdot\hat{\boldsymbol{N}}$. Only the components of $\boldsymbol{t}$ that are non-zero are shown in Table I. When follower load is considered, the constant pressure P that is normal to the given face is provided.

Problems A and B converge to the exact solution using one hexahedral element and $p = 1$ (with no change in the results for higher p-values). For problem D for which stresses are non-homogenous and for problem C which represents a curved domain we provide convergence plots with respect to strain-energy norm as we increase the p-level over a constant mesh (see Figure 3) and using 20 equal load steps. The exact value of the strain energy can be computed using $\int_\Omega \psi(\boldsymbol{C})\mathrm{d}\Omega$ with ψ being the strain-energy density function. The energy norm [12] is defined as $\|\mathscr{U}\| = \sqrt{\int_\Omega \psi(\boldsymbol{C})\mathrm{d}\Omega}$. For comparison, the convergence using the h-FE commercial code Abaqus 6.8 EF is also included using the automatic load step control. The relative error in energy norm is defined as: $\text{Error}\|\mathscr{U}\|\% = ((\|\mathscr{U}_{FE}\| - \|\mathscr{U}_{\text{Exact}}\|)/\|\mathscr{U}_{\text{Exact}}\|)\times 100$ (Figures 4 and 5).

Remark 3.2
Although the state of stress and strain is homogeneous in problem C, the energy norm of the FE solution does not provide an exact solution for $p \geqslant 1$ because of the circular boundary of the domain. The blending-mapping method introduces in this case (through the Jacobian) a rational function in Cartesian coordinates. An increase in the p-level implies an increase in the number of integration points resulting in a better approximation for the numerical computation of the strain energy.

Remark 3.3
An automatic load step algorithm is chosen in Abaqus (h-FEM), resulting in 17 load steps for all the meshes used.

3.1. Problems F and G

For problems F and G we consider the same deformation outlined in Table I for problems A and B, respectively, but now the anisotropic contribution in the form of $\Psi_{1,\text{fibers}}$ is included. The fiber orientation for problems F and G is shown in Figure 6. The anisotropic part results in addition to the traction values outlined in Table I. The tractions resulting from the anisotropic part for problem F are
Face 2 and Face 4:

$$\begin{aligned} t_Y = {} & \{-\tfrac{4}{3}k_1[(\cos^2\beta+\sin^2\beta(\sin^2\phi+a^2\cos^2\phi))^2 a^{-\frac{4}{3}} - (\cos^2\beta+\sin^2\beta(\sin^2\phi+a^2\cos^2\phi))a^{-\frac{2}{3}}] \\ & +4k_1[(\cos^2\beta+\sin^2\beta(\sin^2\phi+a^2\cos^2\phi))a^{-\frac{4}{3}} - a^{-\frac{2}{3}}]\sin^2\beta\sin^2\phi\} \\ & \times e^{k_2((\cos^2\beta+\sin^2\beta(\sin^2\phi+a^2\cos^2\phi))a^{-\frac{2}{3}}-1)^2} \end{aligned} \tag{33}$$

$$\begin{aligned} t_Z = {} & \{-2k_1[(\cos^2\beta+\sin^2\beta(\sin^2\phi+a^2\cos^2\phi))a^{-\frac{1}{3}} - a^{\frac{1}{3}}]\sin^2\beta\sin 2\phi\} \\ & \times e^{k_2((\cos^2\beta+\sin^2\beta(\sin^2\phi+a^2\cos^2\phi))a^{-\frac{2}{3}}-1)^2} \end{aligned}$$

DOI: 10.1002/nme

Table I. Details on problems A–D and the exact solutions.

Problem	Ω_0	Boundary conditions applied to faces F1–F6	Body forces	Solution	Deformation
A	$0\leqslant X\leqslant 2$	$F1: u_X = u_Y = u_Z = 0$	None	$x = X,\ y = Y,\ z = aZ$	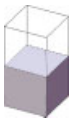
	$0\leqslant Y\leqslant 2$	$F2: t_Y = -(\frac{2}{3}c_1(a^{-\frac{2}{3}} - a^{\frac{4}{3}}) + \frac{2}{D_1}(a^2 - a))$		$u_X = 0$	
	$0\leqslant Z\leqslant 2$	$F3: t_X = \frac{2}{3}c_1(a^{-\frac{2}{3}} - a^{\frac{4}{3}}) + \frac{2}{D_1}(a^2 - a)$		$u_Y = 0$	
		$F4: t_Y = \frac{2}{3}c_1(a^{-\frac{2}{3}} - a^{\frac{4}{3}}) + \frac{2}{D_1}(a^2 - a)$		$u_Z = Z(a-1)$	
		$F5: t_X = -(\frac{2}{3}c_1(a^{-\frac{2}{3}} - a^{\frac{4}{3}}) + \frac{2}{D_1}(a^2 - a))$			
		$F6: t_Z = \frac{4}{3}c_1(a^{\frac{1}{3}} - a^{\frac{5}{3}}) + \frac{2}{D_1}(a-1)$			
B	$0\leqslant X\leqslant 2$	$F1: u_X = u_Y = u_Z = 0$	None	$x = X,\ y = Y + Z\sin(\theta)$	
	$0\leqslant Y\leqslant 2$	$F2: t_Y = -(2c_1(\cos^{-\frac{2}{3}}(\theta) - \cos^{-\frac{8}{3}}(\theta)(1+\sin^2(\theta))) + \frac{2}{D_1}(\frac{\sin(\theta)}{\cos(\theta)} - \sin(\theta) + \cos(\theta) - 1))$		$z = Z\cos(\theta)$	
	$0\leqslant Z\leqslant 2$	$t_Z = -2c_1(\cos^{-\frac{8}{3}}(\theta)\sin(\theta) + \cos^{\frac{1}{3}}(\theta) - \cos^{-\frac{5}{3}}(\theta)) + \frac{2}{D_1}(\frac{\sin(\theta)}{\cos(\theta)} - \sin(\theta) + \cos(\theta) - 1)$		$u_X = 0$	
		$F3: t_X = \frac{2}{D_1}(\cos^2(\theta) - \cos(\theta))$		$u_Y = Z\sin(\theta)$	
		$F4: t_Y = 2c_1(\cos^{-\frac{2}{3}}(\theta) - \cos^{-\frac{8}{3}}(\theta)(1+\sin^2(\theta))) + \frac{2}{D_1}(1 - \cos^{-1}(\theta) + \sin^2(\theta)(\cos^{-1}(\theta) - 1))$		$u_Z = Z(\cos(\theta) - 1)$	
		$t_Z = 2c_1(\cos^{-\frac{8}{3}}(\theta)\sin(\theta) + \cos^{\frac{1}{3}}(\theta) - \cos^{-\frac{5}{3}}(\theta))) + \frac{2}{D_1}(\frac{\sin(\theta)}{\cos(\theta)} - \sin(\theta) + \cos(\theta) - 1))$			
		$F5: t_X = -(\frac{2}{D_1}(\cos^2(\theta) - \cos(\theta)))$			
		$F6: t_Z = 2c_1(\cos^{\frac{1}{3}}(\theta) - \cos^{-\frac{5}{3}}(\theta)) + \frac{2}{D_1}(\cos(\theta) - 1)$			
C	$0\leqslant X\leqslant 10$	$F_1: P = (a^2-1)(\frac{2}{D_1} + \frac{2}{3}c_1 a^{-\frac{10}{3}})$	None	$x = X, y = aY, z = aZ$	
	$\frac{\pi}{2}\leqslant\theta\leqslant\pi$	$F_2: u_Z = 0,\ P = 0$		$u_X = 0$	
	$10\leqslant R\leqslant 20$	$F_3: u_X = 0,\ P = 0$		$u_Y = Y(a-1)$	
	$R = \sqrt{Y^2 + Z^2}$	$F_4: u_Y = 0,\ P = 0$		$u_Z = Z(a-1)$	
		$F_5: u_X = 0,\ P = 0$			
		$F_6: P = (a^2-1)(\frac{2}{D_1} + \frac{2}{3}c_1 a^{-\frac{10}{3}})$			
D	$0\leqslant X\leqslant 2$	$F1: u_X = u_Y = u_Z = 0$	$f_X = 0$	$x = X, y = Y, z = \frac{2}{3}Z^{\frac{3}{2}} + \frac{1}{3}$	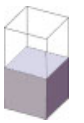
	$0\leqslant Y\leqslant 2$	$F2: t_Y = -(\frac{2}{3}c_1(Z^{-\frac{2}{6}} - Z^{\frac{4}{6}}) + \frac{2}{D_1}(Z - \sqrt{Z}))$	$f_Y = 0$	$u_X = 0$	
	$1\leqslant Z\leqslant 3$	$F3: t_X = \frac{2}{3}c_1(Z^{-\frac{2}{6}} - Z^{\frac{4}{6}}) + \frac{2}{D_1}(Z - \sqrt{Z})$	$f_Z = -\frac{4c_1}{18}Z^{-\frac{4}{3}}$	$u_Y = 0$	
		$F4: t_Y = \frac{2}{3}c_1(Z^{-\frac{2}{6}} - Z^{\frac{4}{6}}) + \frac{2}{D_1}(Z - \sqrt{Z})$	$-\frac{20c_1}{18}Z^{-\frac{7}{3}}$	$u_Z = \frac{2}{3}Z^{\frac{3}{2}} - Z + \frac{1}{3}$	
		$F5: t_X = -(\frac{2}{3}c_1(Z^{-\frac{2}{6}} - Z^{\frac{4}{6}}) + \frac{2}{D_1}(Z - \sqrt{Z}))$	$-\frac{1}{D_1 Z}$		
		$F6: t_Z = \frac{4}{3}c_1(Z^{\frac{1}{6}} - Z^{\frac{5}{6}}) + \frac{2}{D_1}(\sqrt{Z} - 1)$			

DOI: 10.1002/nme

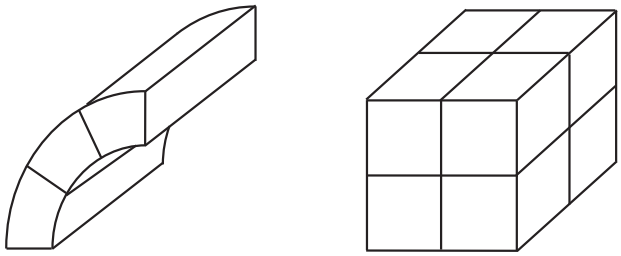

Figure 3. Left: mesh for problem C, right: mesh for problem D.

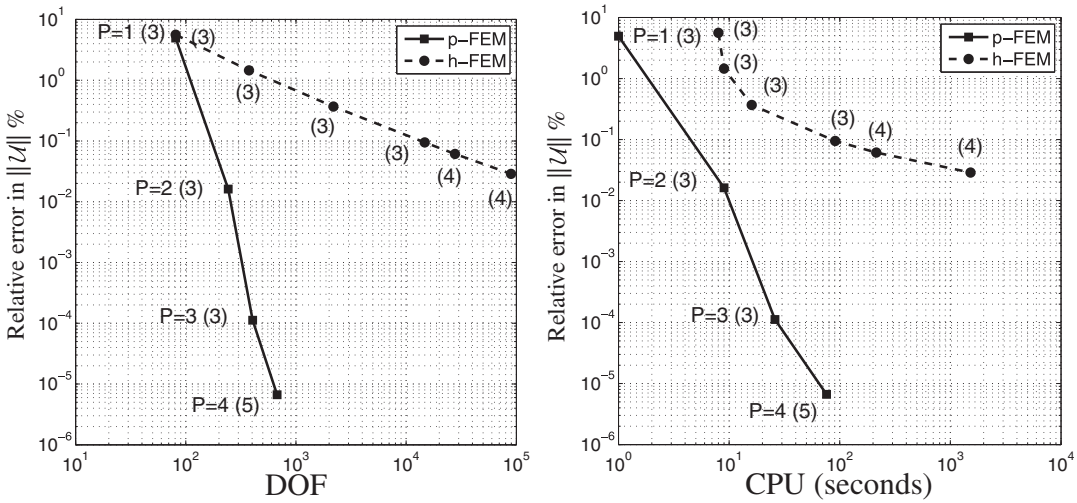

Figure 4. Convergence in energy norm for problem C (average number of equilibrium iterations shown in brackets).

Face 3 and Face 5:

$$t_X = \{-\tfrac{4}{3}k_1[(\cos^2\beta+\sin^2\beta(\sin^2\phi+a^2\cos^2\phi))^2 a^{-\frac{4}{3}} - (\cos^2\beta+\sin^2\beta(\sin^2\phi+a^2\cos^2\phi))a^{-\frac{2}{3}}]$$
$$4k_1[(\cos^2\beta+\sin^2\beta(\sin^2\phi+a^2\cos^2\phi))a^{-\frac{4}{3}} - a^{-\frac{2}{3}}]\cos^2\beta\}$$
$$\times e^{k_2((\cos^2\beta+\sin^2\beta(\sin^2\phi+a^2\cos^2\phi))a^{-\frac{2}{3}}-1)^2} \tag{34}$$

Face 6:

$$t_Z = \{-\tfrac{4}{3}k_1[(\cos^2\beta+\sin^2\beta(\sin^2\phi+a^2\cos^2\phi))^2 a^{-\frac{7}{3}} - (\cos^2\beta+\sin^2\beta(\sin^2\phi+a^2\cos^2\phi))a^{-\frac{5}{3}}]$$
$$+4k_1[(\cos^2\beta+\sin^2\beta(\sin^2\phi+a^2\cos^2\phi))a^{-\frac{7}{3}} - a^{-\frac{5}{3}}]\sin^2\beta\cos^2\phi\}$$
$$\times e^{k_2((\cos^2\beta+\sin^2\beta(\sin^2\phi+a^2\cos^2\phi))a^{-\frac{2}{3}}-1)^2} \tag{35}$$

$$t_Y = \{-2k_1[(\cos^2\beta+\sin^2\beta(\sin^2\phi+a^2\cos^2\phi))a^{-\frac{4}{3}} - a^{-\frac{2}{3}}]\sin^2\beta\sin 2\phi\}$$
$$\times e^{k_2((\cos^2\beta+\sin^2\beta(\sin^2\phi+a^2\cos^2\phi))a^{-\frac{2}{3}}-1)^2}$$

DOI: 10.1002/nme

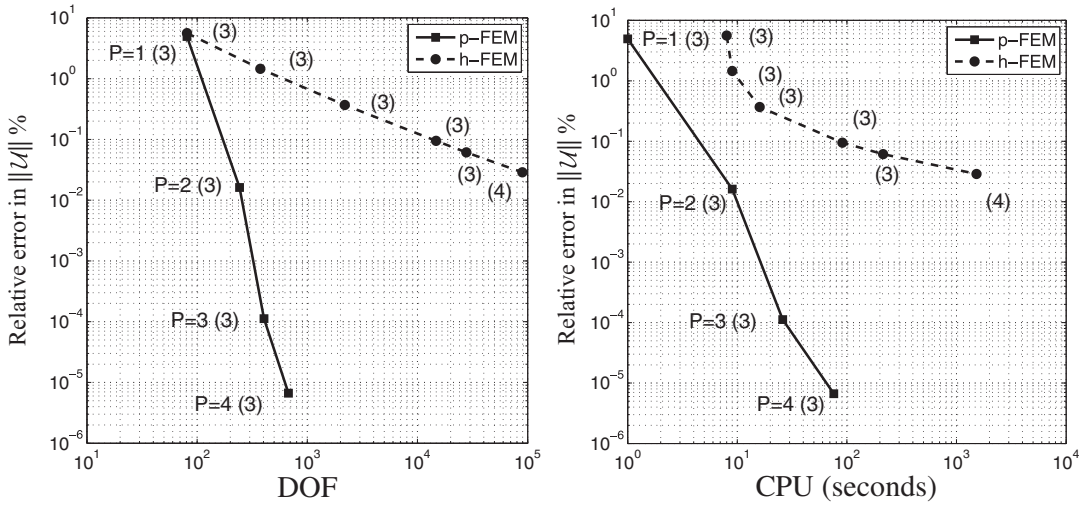

Figure 5. Convergence in energy norm for problem D (average number of equilibrium iterations shown in brackets).

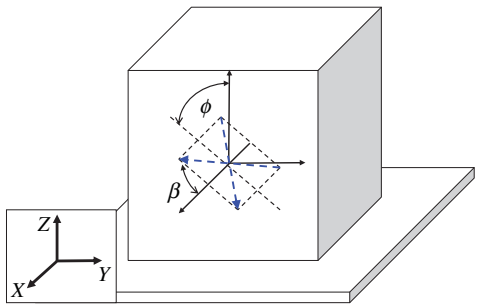

Figure 6. Initial fiber family orientation for the anisotropic Neo-Hookean example problems.

The tractions resulting from the anisotropic part for problem G are:
Face 2 and Face 4:

$$
\begin{aligned}
t_Y = \{&-\tfrac{4}{3}k_1[(\cos^2\beta+\sin^2\beta(1-\sin 2\phi\sin\theta))^2\cos^{-\frac{10}{3}}\theta-(\cos^2\beta+\sin^2\beta(1-\sin 2\phi\sin\theta))\cos^{-\frac{8}{3}}\theta]\\
&+4k_1[(\cos^2\beta+\sin^2\beta(1-\sin 2\phi\sin\theta))\cos^{-\frac{4}{3}}\theta-\cos^{-\frac{2}{3}}\theta]\sin^2\beta\sin^2\phi\}\\
&\times e^{k_2((\cos^2\beta+\sin^2\beta(1-\sin 2\phi\sin\theta))\cos^{-\frac{2}{3}}-1)^2}\\
t_Z = \{&\tfrac{4}{3}k_1[(\cos^2\beta+\sin^2\beta(1-\sin 2\phi\sin\theta))\cos^{-\frac{10}{3}}\theta\sin\theta\\
&-(\cos^2\beta+\sin^2\beta(1-\sin 2\phi\sin\theta))\cos^{-\frac{8}{3}}\theta\sin\theta]\\
&-4k_1[(\cos^2\beta+\sin^2\beta(1-\sin 2\phi\sin\theta))\cos^{-\frac{4}{3}}\theta-\cos^{-\frac{2}{3}}\theta]\sin^2\beta\sin\phi\cos\phi\}\\
&\times e^{k_2((\cos^2\beta+\sin^2\beta(1-\sin 2\phi\sin\theta))\cos^{-\frac{2}{3}}-1)^2}
\end{aligned}
\tag{36}
$$

DOI: 10.1002/nme

Face 3 and Face 5:

$$t_X = \{-\tfrac{4}{3}k_1[(\cos^2\beta+\sin^2\beta(1-\sin 2\phi\sin\theta))^2\cos^{-\frac{4}{3}}\theta-(\cos^2\beta+\sin^2\beta(1-\sin 2\phi\sin\theta))\cos^{-\frac{2}{3}}\theta]$$
$$+4k_1[(\cos^2\beta+\sin^2\beta(1-\sin 2\phi\sin\theta))\cos^{-\frac{4}{3}}\theta-\cos^{-\frac{2}{3}}\theta]\cos^2\beta\}$$
$$\times e^{k_2((\cos^2\beta+\sin^2\beta(1-\sin 2\phi\sin\theta))\cos^{-\frac{2}{3}}-1)^2} \tag{37}$$

Face 6:

$$t_Z = [\{-\tfrac{4}{3}k_1[(\cos^2\beta+\sin^2\beta(1-\sin 2\phi\sin\theta))^2\cos^{-\frac{10}{3}}\theta\sin\theta-(\cos^2\beta+\sin^2\beta(1-\sin 2\phi\sin\theta))$$
$$\times\cos^{-\frac{8}{3}}\theta\sin\theta]+[(\cos^2\beta+\sin^2\beta(1-\sin 2\phi\sin\theta))\cos^{-\frac{4}{3}}\theta\sin\theta-\cos^{-\frac{2}{3}}\theta\sin\theta]\sin^2\beta\sin^2\phi\}$$
$$+\{\tfrac{4}{3}k_1[(\cos^2\beta+\sin^2\beta(1-\sin 2\phi\sin\theta))^2\cos^{-\frac{10}{3}}\theta\sin\theta-(\cos^2\beta+\sin^2\beta(1-\sin 2\phi\sin\theta))$$
$$\times\cos^{-\frac{8}{3}}\theta\sin\theta]-4k_1[(\cos^2\beta+\sin^2\beta(1-\sin 2\phi\sin\theta))\cos^{-\frac{7}{3}}\theta-\cos^{-\frac{5}{3}}\theta]\sin^2\beta\sin\phi\cos\phi\}]$$
$$\times e^{k_2((\cos^2\beta+\sin^2\beta(1-\sin 2\phi\sin\theta))\cos^{-\frac{2}{3}}-1)^2} \tag{38}$$

$$t_Y = [\{\tfrac{4}{3}k_1[(\cos^2\beta+\sin^2\beta(1-\sin 2\phi\sin\theta))^2\cos^{-\frac{7}{3}}\theta-(\cos^2\beta+\sin^2\beta(1-\sin 2\phi\sin\theta))\cos^{-\frac{5}{3}}\theta]$$
$$+4k_1[(\cos^2\beta+\sin^2\beta(1-\sin 2\phi\sin\theta))\cos^{-\frac{1}{3}}\theta-\cos^{\frac{1}{3}}\theta]\sin^2\beta\cos^2\phi\}$$
$$+\{\tfrac{4}{3}k_1[(\cos^2\beta+\sin^2\beta(1-\sin 2\phi\sin\theta))^2\cos^{-\frac{10}{3}}\theta\sin\theta-(\cos^2\beta+\sin^2\beta(1-\sin 2\phi\sin\theta))$$
$$\times\cos^{-\frac{8}{3}}\theta\sin\theta]-4k_1[(\cos^2\beta+\sin^2\beta(1-\sin 2\phi\sin\theta))\cos^{-\frac{4}{3}}\theta-\cos^{-\frac{2}{3}}\theta]\sin^2\beta\sin\phi\cos\phi\sin\theta\}]$$
$$\times e^{k_2((\cos^2\beta+\sin^2\beta(1-\sin 2\phi\sin\theta))\cos^{-\frac{2}{3}}-1)^2}$$

The values of the deformation parameters $a=1-2$, $\theta=0-40^\circ$ were examined for different fiber orientation angles $\phi=0-90^\circ$, $\beta=0-90^\circ$ and the exact solution was obtained using one hexahedral element with $p=1$ (with no change in the results for higher p-values).

4. AN EXAMPLE REPRESENTING A TYPICAL ARTERY

Following the verification of the p-FE implementation, we demonstrate its performance by simulating the passive arterial response of the human LAD coronary artery. Both mono-layered (media only) and bi-layered models (media and adventitia) are considered. The material parameters for (8) and (9) used in our analysis were fitted in [14] to experimental data on the human LAD coronary artery reported in [15]. In [14], the incompressible limit of (8) and (9) was considered by fitting the material parameters, therefore in our computations a small value of $D_1=0.01\,\mathrm{MPa}^{-1}$ was used so

Table II. Material parameters fitted to (8) and (9) for LAD human coronary arteries from [14] for experiments reported in [15].

Layer	c_1 (kPa)	k_1 (kPa)	k_2	β (°)	R_{in} (mm)	R_{out} (mm)
Media	27	0.64	3.54	10	3.3170	3.8103
Adventitia	2.7	5.1	15.4	40	3.8103	4.0570

DOI: 10.1002/nme

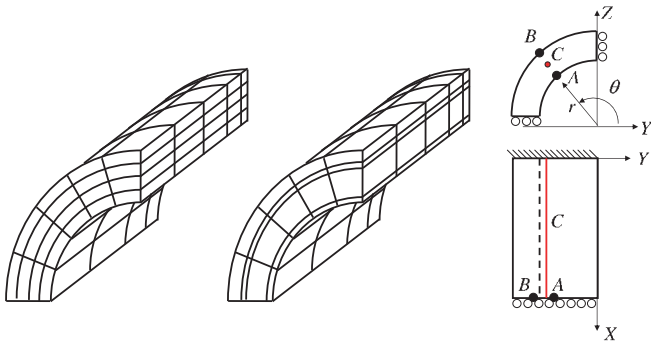

Figure 7. 'Benchmark' problem—mesh used: Left—mono-layer, bi-layered. Right—boundary conditions and data extraction points A, B and along line C.

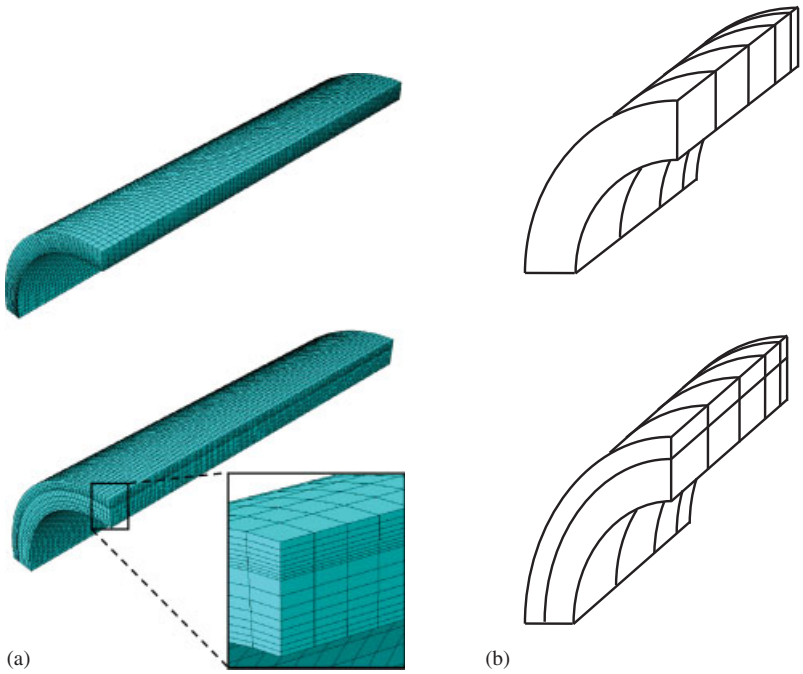

Figure 8. Meshes used in the LAD analysis: (a) Abaqus and (b) p-FE. Top–mono-layer and bottom—bi-layered.

as to ensure that $J-1=\triangle V/V\approx 0.001\%$. The artery was modeled as a tube of length $L=20\,\text{mm}$, clamped at both ends and loaded by an internal pressure of $P=13.3\,\text{kPa}$ (100 mmHg). The material parameters for each layer and inner and outer radii are given in Table II. Owing to problem's symmetry, only 1/8 of the tube was modeled with symmetry boundary conditions applied as shown in Figure 7. To investigate the performance of the p-FEM with respect to the traditional h-FEMs, a benchmark solution to which the computations can be compared is required. The 'benchmark' solution was obtained using a graded mesh of 100 hexahedral elements (shown in Figure 7) with p-extension $p=1-8$ having at $p=8$ 54 720 DOFs. Twenty equal load steps were used for each p-extension. The benchmark problems (mono- and bi-materials) were also solved using the h-FE commercial code Abaqus 6.8 EF as well as our p-FE implementation. An example of the graded meshes used in Abaqus and our code is shown in Figure 8. For the h-FE mesh a maximum aspect ratio of 1:4 is observed to reduce numerical errors, thus a large number of elements are obtained for thin-layered structures such as the artery wall (see Figure 8). Eight-noded hexahedral hybrid

DOI: 10.1002/nme

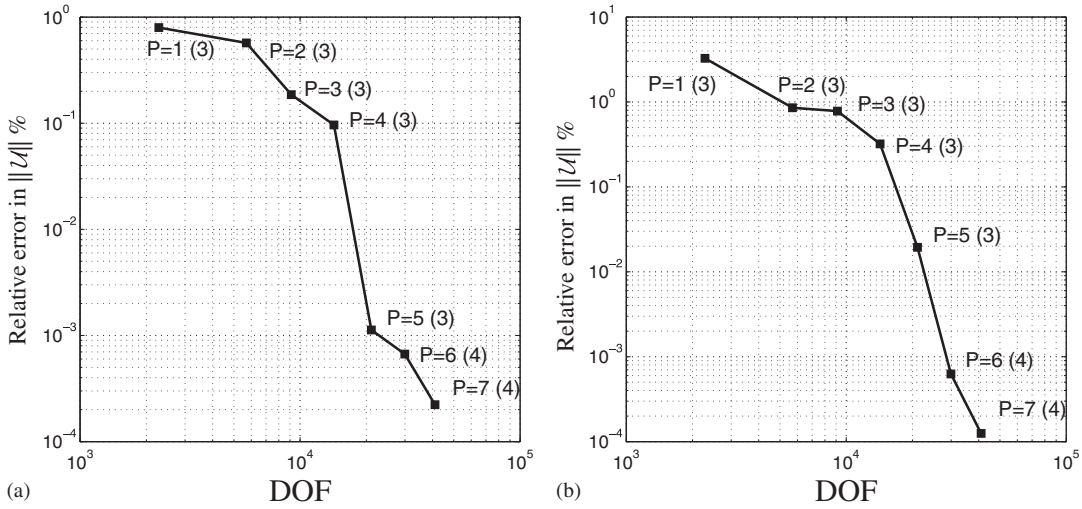

Figure 9. Convergence in energy norm for the LAD coronary (average number of equilibrium iterations shown in brackets): (a) mono-layer and (b) bi-layer.

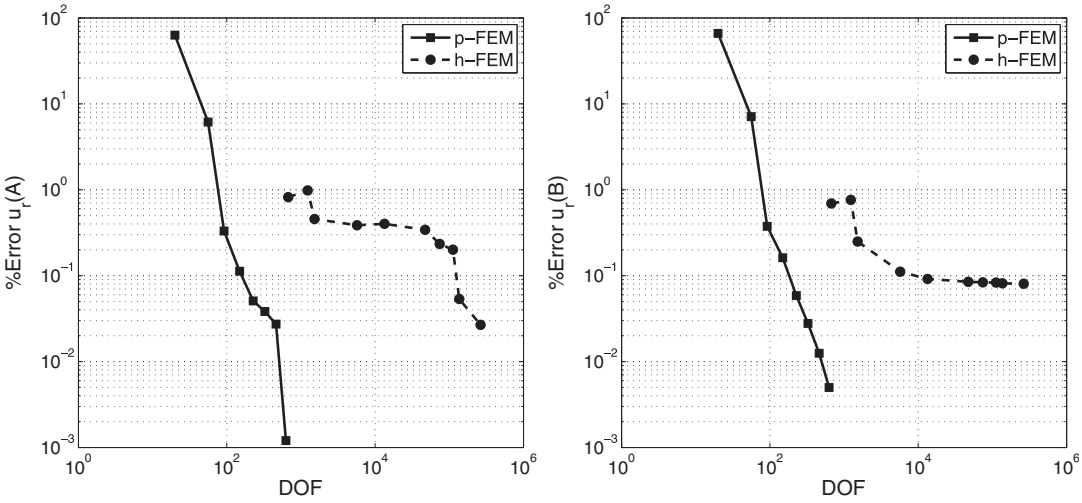

Figure 10. Convergence of u_r at point A (left) and point B (right)—mono-layered problem.

elements were used in Abaqus due to the incompressibility constraint (20-noded quadratic brick elements were also tested showing the same efficiency as the 8-noded ones) and automatic load step control was utilized in the non-linear iterative scheme. In the p-FE code standard hexahedral elements were used with 20 equal load steps.

Convergence in strain energy for the 'benchmark' solution is shown in Figure 9.

The mono-layer model: In Figures 10–13, a comparison of the convergence as a function of DOF and CPU for radial displacement and circumferential stress extracted at points A and B (see Figure 7) is shown. In Figure 14, the relative error in percentage in circumferential stress $\|((\sigma_{\theta\theta}^{\text{Benchmark}} - \sigma_{\theta\theta}^{p})/\sigma_{\theta\theta}^{\text{Benchmark}}) \times 100\|$ along line C (X, $R = (R_{\text{in}} + R_{\text{out}})/2$, $\theta = 135^{\circ}$, see Figure 7) is plotted with the 'Benchmark' solution used for estimation of the error. As expected the error increases for values computed close to the clamped BCs at $x = 0$.

The bi-layer model: In Figures 15–18, the convergence patterns of the radial displacement and circumferential stress are presented.

DOI: 10.1002/nme

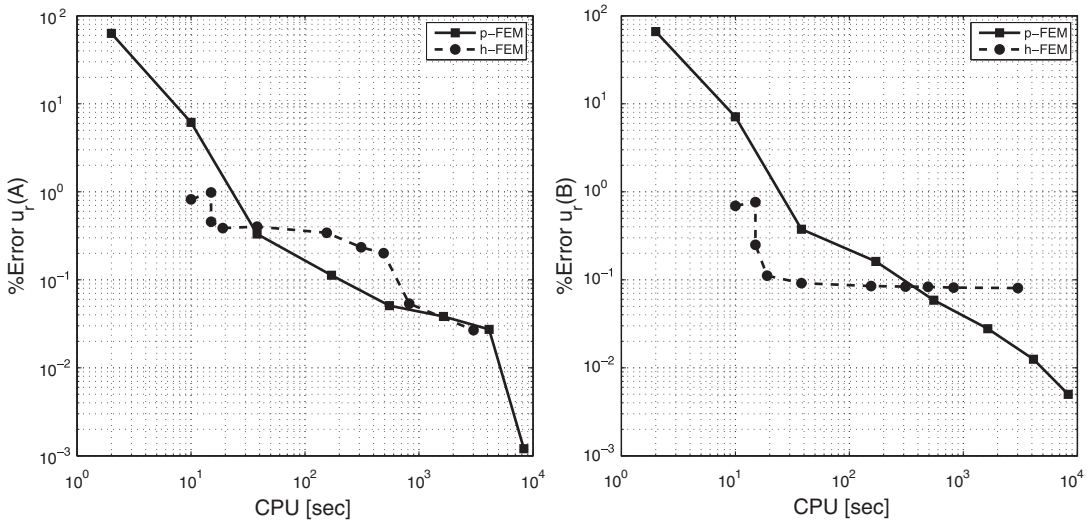

Figure 11. Convergence in terms of CPU of u_r at point A (left) and point B (right)—mono-layered problem.

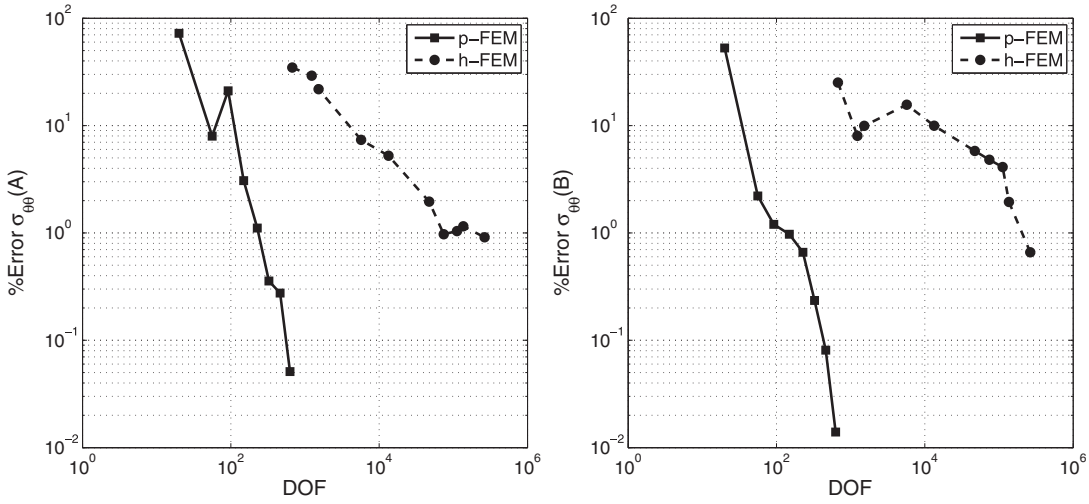

Figure 12. Convergence of $\sigma_{\theta\theta}$ at point A (left) and point B (right)—mono-layered problem.

The results demonstrate that the convergence rates of the p-FEMs with respect to DOFs are much faster compared to their h-FEM counterparts. This is especially important when modeling a general artery constructed from multiple thin layers. In terms of CPU, our p-FEM implementation is so far non-optimal and does not account for the bandwidth of the generated overall stiffness matrix. Nevertheless, computational time is shorter for a sequence of solutions to verify convergence.

4.1. Numerical investigation on the effect of fiber model and influence of incompressibility

As noted, two SEDFs representing the fiber families $\Psi_{1,\text{fibers}}$ and $\Psi_{2,\text{fibers}}$ are documented in the literature. To study the difference between the SEDF's at the limit of incompressibility a numerical investigation was conducted using the mono-layer artery problem described previously. The problem was solved using either $\Psi_{1,\text{fibers}}$ or $\Psi_{2,\text{fibers}}$.

DOI: 10.1002/nme

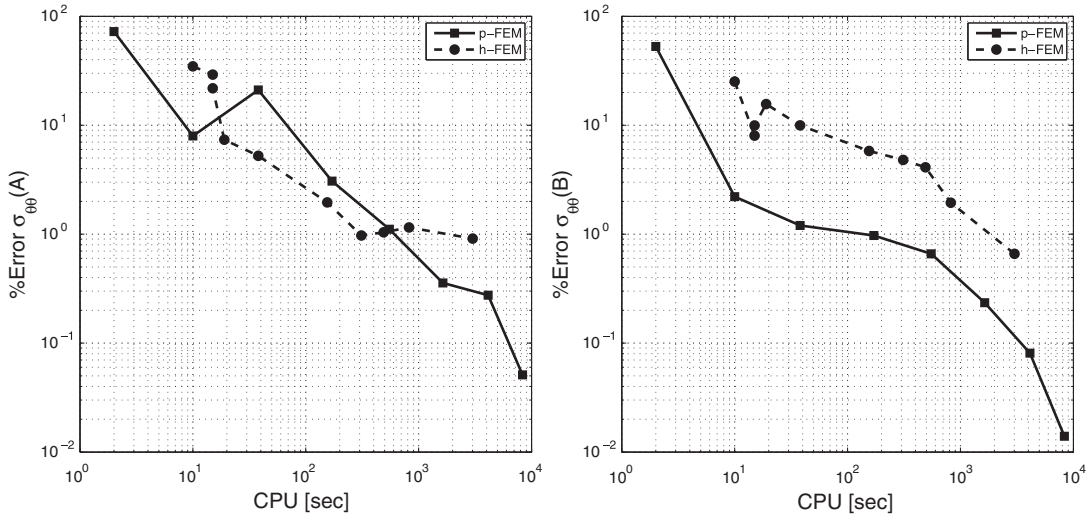

Figure 13. Convergence in terms of CPU of $\sigma_{\theta\theta}$ at point A (feft) and point B (right)—mono-layered problem.

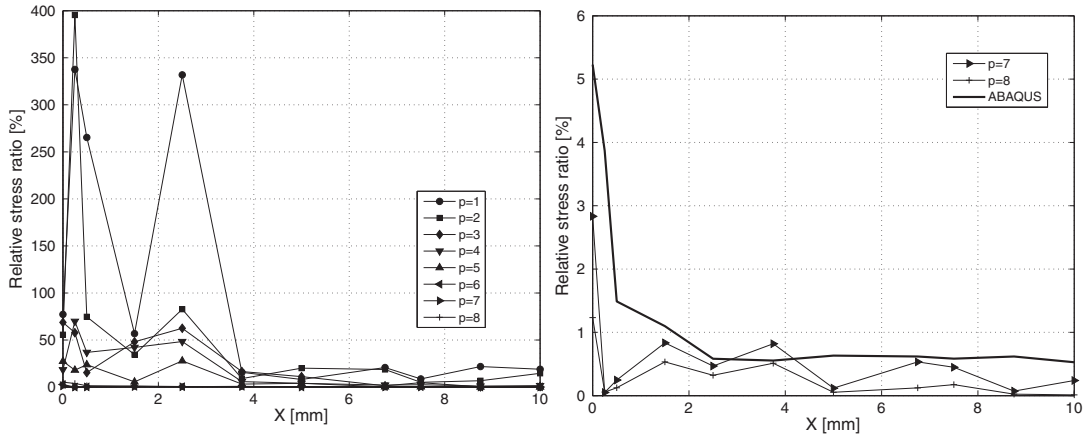

Figure 14. Mono-layered model: relative error in circumferential stress along line C for different p-extensions: left—$p=1-8$ and right—zoom for $p=7-8$, ABAQUS (61 200 elements).

Remark 4.1

To obtain the incompressible limit case, small values of D_1 were taken but due to the different constitutive models, the two SEDFs yield different $\Delta V/V$ ratios for same D_1 value and pressure. To obtain $\Delta V/V<0.001\%$, $D_1=0.01\,\mathrm{MPa}^{-1}$ was chosen for both $\Psi_{1,\mathrm{fibers}}$ and $\Psi_{2,\mathrm{fibers}}$.

We plot the arterial deformation and the relative difference in radius and circumferential stress in percentage $((R_{\mathrm{mid}}^{\Psi_{1,\mathrm{fibers}}}-R_{\mathrm{mid}}^{\Psi_{2,\mathrm{fibers}}})/R_{\mathrm{mid}}^{\Psi_{1,\mathrm{fibers}}})\times 100$ and $((\sigma_{\theta\theta}(R_{\mathrm{mid}})^{\psi_{1,\mathrm{fibers}}}-\sigma_{\theta\theta}(R_{\mathrm{mid}})^{\psi_{2,\mathrm{fibers}}})/\sigma_{\theta\theta}(R_{\mathrm{mid}})^{\psi_{1,\mathrm{fibers}}})\times 100$ along the arterial axis in Figure 19. As noticed in Figure 19, at the incompressible limit there is no notable difference in computed displacement or stress. When increasing the compressibility $\Delta V/V\approx 3\%$ the average relative difference along the arterial axis is increased to about 11.5 and 12.6% for the radius and stress, respectively.

The effect of the compressibility (the value of D_1 and applied pressure) on the mechanical response was investigated on the same mono-layer (media only) model for the LAD coronary artery. The material parameters and dimensions of the artery are given in Table II ($c_1=27\,\mathrm{kPa}$,

DOI: 10.1002/nme

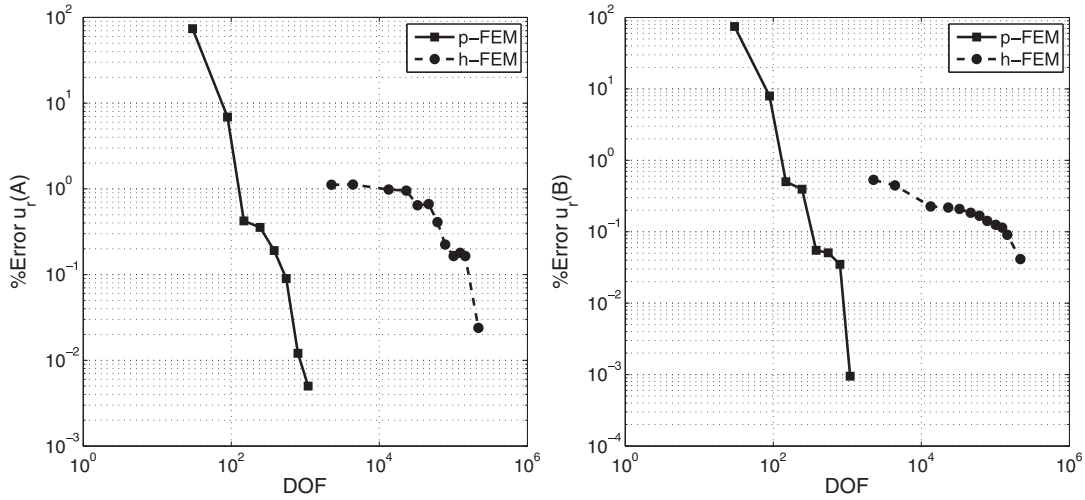

Figure 15. Convergence of u_r at point A (left) and point B (right)—i-layered problem.

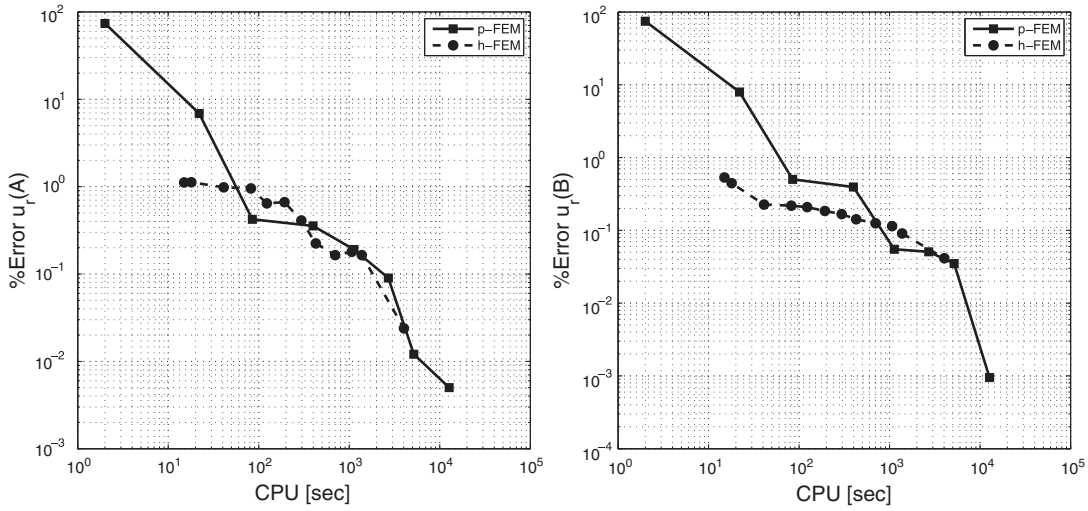

Figure 16. Convergence in terms of CPU of u_r at point A (left) and point B (right)—i-layered problem.

$k_1 = 0.64\,\text{kPa}, k_2 = 3.54, \beta = 10, R_{\text{in}} = 3.3170\,\text{mm}, R_{\text{out}} = 3.8103\,\text{mm}$) and the p-FE mesh is shown in the upper right corner of Figure 8.

A pressure of $P = 13.3\,\text{kPa}$ (100 mmHg) is applied on the internal surface of the artery and the radial displacement and circumferential stress across the thickness between points A and B in Figure 8 are monitored. The problems are solved using $p = 1-8$ for each of the five values of $D_1 = 3, 1, 0.5, 0.1, 0.01\,\text{MPa}^{-1}$. In Table III, we summarize the relative volume change $\Delta V/V$ (%) for each value of D_1 as p increases. In Figure 20, we plot the value of radial displacement and circumferential stress across the artery thickness. As seen in Figure 20, even a small level of compressibility of the tissue $\triangle V/V \approx 3\%$ results in a 30% drop of the circumferential stress value at the inner boundary and an increase of 18% at the outer boundary. This phenomenon is highly correlated with findings in biological systems, shown to have evolutionary adaptation so as to level off the stress gradients. This suggests that the assumption of artery

DOI: 10.1002/nme

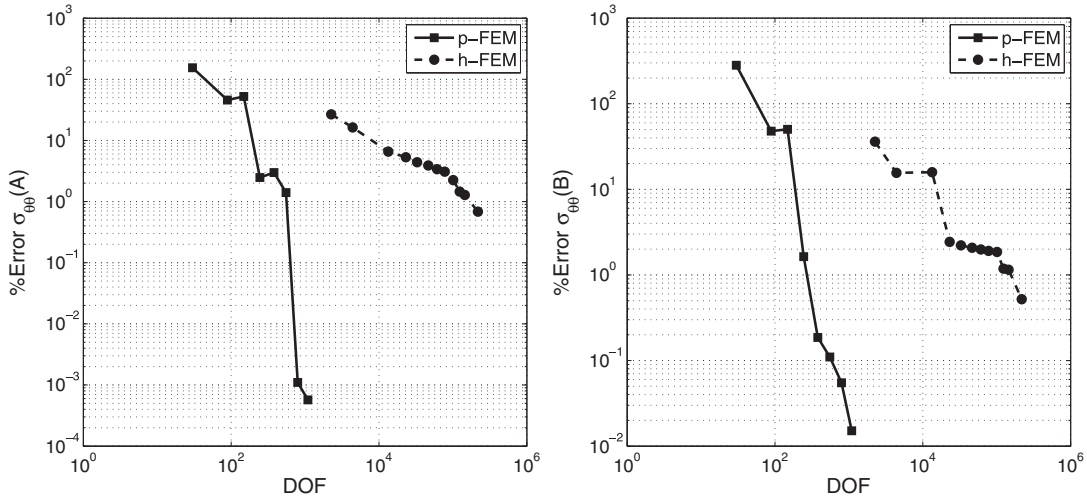

Figure 17. Convergence of $\sigma_{\theta\theta}$ at point A (left) and point B (right)—bi-layered problem.

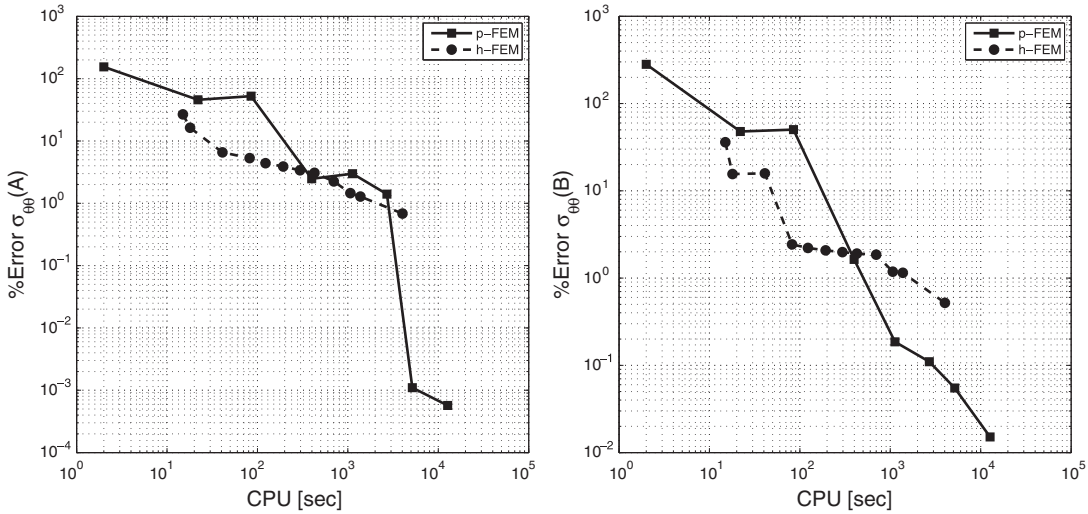

Figure 18. Convergence in terms of CPU of $\sigma_{\theta\theta}$ at point A (left) and point B (right)—bi-layered problem.

incompressibility may not well represent the reality well and should be carefully examined in future works.

Remark 4.2

It should be noted that all computations were performed using material parameters that were fitted for the incompressible model as in [14]. Fitting material parameters to a compressible model should be conducted if one wishes to study in more depth the compressible case.

Remark 4.3

The isotropic part of the SEDF in (7) may result in a 'non-physical' mechanical behavior for $\kappa/\mu \equiv (2/c_1 D_1) < (2/3)$ for uniaxial stretches larger than a certain value (see [16, p. 87] and [9] for details). In Appendix A it is demonstrated that the value of $D_1 = 1$, which corresponds to a relative volume change of 3% under physiological pressure and a stretch ratio of about 1.5, does result in a 'reasonable physical' mechanical response.

DOI: 10.1002/nme

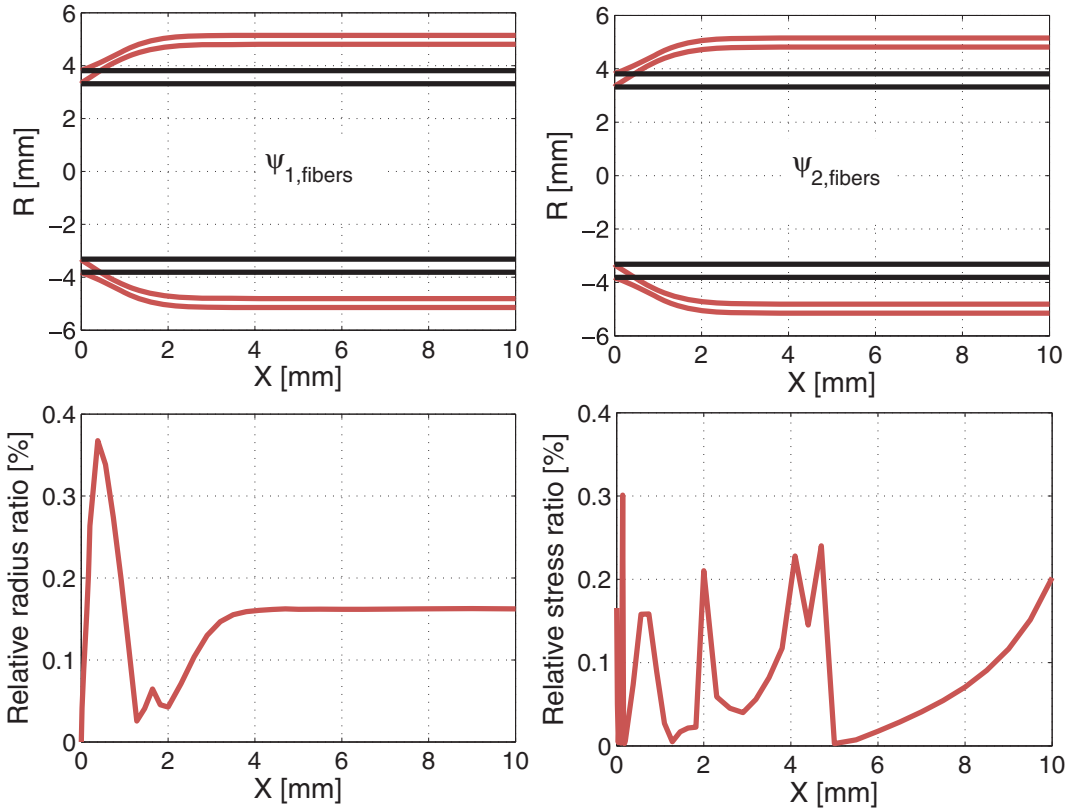

Figure 19. Deformation of the mono-layer 'artery' and relative difference in radius and circumferential stress for the different fiber models along the artery axis ($R_{\text{mid}} = (R_{\text{out}} + R_{in})/2$, $\Delta V/V \approx 0.001\%$).

Table III. Relative volume change $\triangle V/V$ (%) for different D_1 values, $P = 13.3\,\text{kPa}$ (100 mmHg).

p	$D_1 = 3$	$D_1 = 1$	$D_1 = 0.5$	$D_1 = 0.1$	$D_1 = 0.01$
1	8.51	2.32	1.20	0.22	0.00099
2	8.96	2.58	1.31	0.26	0.00099
3	8.37	2.71	1.37	0.27	0.00099
4	8.16	2.77	1.40	0.27	0.00050
5	8.04	2.74	1.44	0.28	0.00041
6	8.34	2.86	1.45	0.28	0.0011
7	8.54	2.87	1.46	0.28	0.0012
8	8.54	2.87	1.46	0.28	0.0012

5. SUMMARY AND CONCLUSIONS

The p-version of the finite element method was extended to model hyper-elastic anisotropic 'artery-like' structures. Based on several analytical and benchmark problems for hyper-elastic isotropic and anisotropic materials, we verified the p-FE implementation and demonstrated that it is much more efficient compared to the h-FEM in terms of number of degrees of freedom as well as CPU times. The performance of the p-FEM for general nearly incompressible (at the incompressible limit case) mono-layered and multi-layered 'artery-like' structures was investigated and compared to the conventional h-FEM (Abaqus 6.8 EF) demonstrating that the displacement-formulation in the

DOI: 10.1002/nme

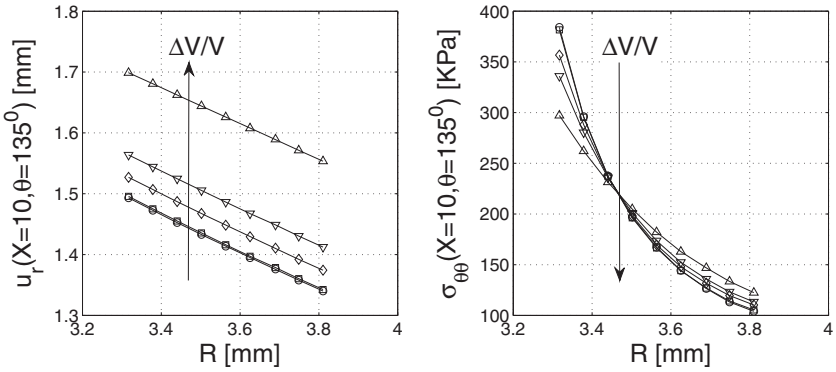

Figure 20. Radial displacement and circumferential stress across the artery thickness for different compressibility values.

context of the p-FEM needs no special treatment for thin-layered nearly incompressible domains. These features make p-FEMs preferred for investigating the mechanical response of the arterial wall. A comparative study of two known SEDF's for modeling the collagen fiber contribution was also performed showing that at the incompressible limit case the two SEDFs result in almost similar mechanical response. However, when slight compressibility is considered, a notable difference is observed. It is still an open question which of the two fiber models best describes the arterial wall passive mechanical response when slight compressibility is taken into account. Further experimental study in conjunction with numerical modeling is required to provide a definitive answer. The effect of arterial compressibility (in light of experimental evidence suggesting a slightly compressibility of the artery wall) was investigated demonstrating that a mild compressibility $\triangle V/V \approx 3\%$ may result in notable difference in values of radial displacement and circumferential stress.

Once the p-FE implementation has been verified and its efficiency was established, it will be used for further on research to further investigate the effect of arterial compressibility on the estimation of SEDF's parameters in (7) and (9) or (10), and assess its performance on realistic models of the human arteries.

APPENDIX A: VERIFICATION OF THE 'PHYSICAL' MECHANICAL RESPONSE FOR THE COMPRESSIBLE SEDF

We herein verify that the compressibility parameters D_1 used in Section 4.1 result in 'physical' mechanical response. Consider a uniaxial tension of a strip representing the media layer of the human LAD coronary artery. We use the material parameters as in Section 4.1 ($c_1 = 27\,\text{kPa}, k_1 = 0.64\,\text{kPa}, k_2 = 3.54, \beta = 10, L = 12\,\text{mm}, W = 4\,\text{mm}, H = 1\,\text{mm}$) with D_1 increasing up to the value of $D_1 = 3\,\text{kPa}$. Owing to symmetry only an eight of the strip was modeled with symmetry boundary conditions prescribed as shown in Figure A1. Because the boundary conditions imply a homogenous deformation, one hexahedral element was used in our computations with ($p = 1$). The uniaxial tension was increased so to obtain a uniaxial stretch ratio in the physiological range up to $\lambda_Y \approx 1.8$, and the lateral stretch ratios were computed. In Figure A2, we plot λ_Y vs λ_X and λ_Z for increasing stretch values for $D_1 = 1, 3$. 'Non-physical' mechanical response is obtained when transverse stretches are larger than 1 ($\lambda_x, \lambda_z > 1$) for $\lambda_y > 1$ (this is equivalent to a negative Poisson's ratio in linear elasticity at the limit when strains and deformations are small). As evident from Figure A2 a 'reasonable physical response' is obtained for the range of physiological stretches $\lambda_y < 1.7$ using the largest D_1 value in our compressibility investigation.

DOI: 10.1002/nme

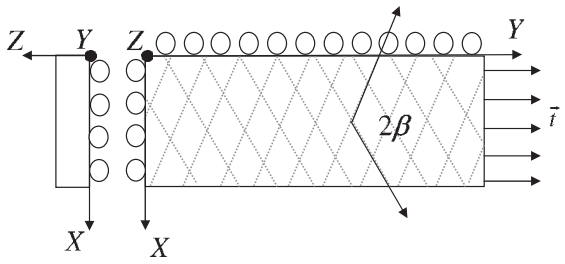

Figure A1. Model for uniaxial tension of a strip made of the media layer of the LAD coronary artery.

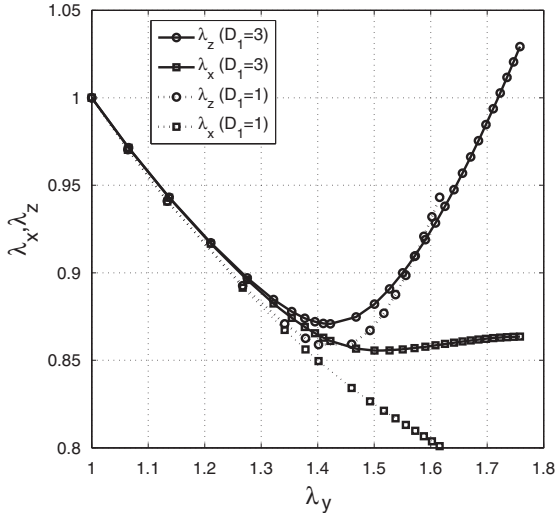

Figure A2. Transverse stretches vs the uniaxial stretch for $D_1 = 1, 3$.

ACKNOWLEDGEMENTS

The authors thank prof. Stefan Hartmann from the TU-Clausthal, Germany for helpful discussions related to nearly incompressible hyperelasticity.

REFERENCES

1. Düster A, Hartmann S, Rank E. p-FEM applied to finite isotropic hyperelastic bodies. *Computer Methods in Applied Mechanics and Engineering* 2003; **192**:5147–5166.
2. Yosibash Z, Hartmann S, Heisserer U, Duester A, Rank E, Szanto M. Axisymmetric pressure boundary loading for finite deformation analysis using p-FEM. *Computer Methods in Applied Mechanics and Engineering* 2007; **196**:1261–1277.
3. Heisserer U, Hartmann S, Düster A, Yosibash Z. On volumetric locking-free behavior of p-version finite elements under finite deformations. *Communications in Numerical Methods in Engineering* 2008; **24**(11):1019–1032.
4. Holzapfel GA, Gasser TC, Ogden RW. A new constitutive framework for arterial wall mechanics and a comparative study of material models. *Journal of Elasticity* 2000; **61**:1–48.
5. Holzapfel GA, Ogden RW. Constitutive modelling of arteries. *Proceedings of the Royal Society A* 2010; **466**: 1551–1597.
6. Carew TE, Vaishnav RN, Patel DJ. Compressibility of the arterial wall. *Circulation Research* 1968; **23**:61–68.
7. Chuong CJ, Fung YC. Compressibility and constitutive equation of arterial wall in radial compression experiments. *Journal of Biomechanics* 1984; **17**(1):35–40.
8. Karlsson Hibbitt and Sorensen Inc. *ABAQUS Manual Version 6.82EF*, 2009.
9. Hartmann S, Neff P. Polyconvexity of generalized polynomial-type hyperelastic strain energy functions for near-incompressibility. *International Journal of Solids and Structures* 2003; **40**(11):2767–2791.
10. Bonet J, Wood RD. *Nonlinear Continuum Mechanics for Finite Element Analysis*. Cambridge University Press: U.S.A., 1997.

DOI: 10.1002/nme

11. Duster A. High order finite elements for three dimensional, thin-walled nonlinear continua. *Ph.D. Thesis*, Technische Universität München, Munich, Germany, 2001.
12. Szabó BA, Babuška I. *Finite Element Analysis*. Wiley: New York, 1991.
13. Press WH, Flannery BP, Teukolsky SA, Vetterling WT. *Numerical Recipes*: *The Art of Scientific Computing*. Cambridge University Press: Cambridge, 1986.
14. Gasser TC, Schulz-Bauer CAJ, Holzapfel GA. A three dimensional finite element model for arterial clamping. *Journal of Biomechanical Engineering* 2002; **124**:355–363.
15. Carmines DV, McElhaney JH, Stack R. A piecewise non-linear elastic stress-expression of human and pig coronary arteries tested in-vitro. *Journal of Biomechanics* 1991; **24**:899–906.
16. Hartmann S. Finite-elemente berechnung inelastischer kontinua. *Habilitation Thesis*, Berichte des Instituts fur Mechanick, Kassel University, Kassel, Germany, 2003.

DOI: 10.1002/nme